Evaluation of marine dredged sediment as reactive powder compared to ground basaltic pyroclastic materials for the development of eco-friendly lime-pozzolan binders

Salim Kourtaa, Morgan Chabannes, Frédéric Becquart, Nor-Edine Abriak

Evaluation of marine dredged sediment as reactive powder compared to ground basaltic pyroclastic materials for the development of eco-friendly lime-pozzolan binders

Salim Kourtaa[1,2], Morgan Chabannes[1,2,*], Frédéric Becquart[1,2], Nor-Edine Abriak[1,2]

[1]IMT Nord Europe, Institut Mines-Télécom, Centre for Materials and Processes, F-59000 Lille, France
[2]Univ. Lille, Institut Mines-Télécom, ULR 4515 – LGCgE, Laboratoire de Génie Civil et géo-Environnement, F-59000 Lille, France

*Corresponding author: morgan.chabannes@imt-nord-europe.fr

Abstract

The combination of lime with natural pozzolans for the production of binders in masonry construction dates back to ancient times. These were largely ignored with the industrialization of the building sector even though their use for specific applications is of interest. The use of lime-pozzolan binders with the least amount of lime is a relevant opportunity to reduce carbon emissions due to the decarbonation of limestone for the production of quicklime but also to introduce new alumino-silicate materials. In this context, the present investigation intends to relate marine dredged sediment to pyroclastic materials and to mix it with hydrated lime without any thermal treatment but after micronization. The blends were moist cured either at 20°C or 50°C and the paper will discuss the pozzolanic reactivity through the study of compressive strength and reaction kinetics from 3 days to 180 days. Reaction product assemblage, microstructure, and porosity refinement were also addressed after advanced curing ages. Results have well illustrated the long-term pozzolanic reactivity of the marine sediment cured at 50°C through the whole combination of initially available lime after 60 days and the compressive strength development providing 12 MPa after 180 days.

Key-words:
Marine dredged sediment;
Basaltic pyroclastic materials;
Pozzolanic reactivity;
Low-carbon binder;
Curing temperature;
Hydration kinetics.

1. Introduction

After World War II, in a context of industrialized and quick production of new buildings, embodied carbon and energy efficiency are relegated to the background. From the mid-1970s, interior insulation of buildings using mineral wools or polystyrene with concrete blocks and other masonry units (such as burnt clay bricks) is widely used in France. These design practices are not the most effective to deal appropriately with moisture condensation and summer thermal comfort which can imply an excessive use of air conditioning. However, these issues were better addressed with ancestral buildings using traditional methods (earth-straw, building stones, etc.). In addition, as a result of successive thermal regulations, a significant part of the overall carbon footprint of buildings is due to the production of materials.

The combination of hydrated lime with natural pozzolans (i.e. pyroclastic fall deposits) goes back to the Greco-Roman period [1]. Unfortunately, the use of lime-pozzolan binders was strongly reduced following the advent of ordinary Portland cement. Furthermore, most natural pozzolans do not present the appropriate properties for specific applications owing to their low reactivity or unstable quality [2]. Nevertheless, some research studies dealing with the use of lime-pozzolan binders for the design of Bio-aggregate-based Building Materials (BBMs) are available [3,4]. Nozahic et al. [3] used trachytic pumice as a natural pozzolan with hydrated lime and some authors [4] used metakaolin (an artificial pozzolan) with various limes bearing in mind the goal of reducing the carbon impact of the binder that will be mixed with plant aggregates (like hemp shives). As a matter of fact, the extraction of raw materials and the production of the lime-based binder are reported to heavily contribute to the carbon footprint of hemp concrete [5,6]. Since carbon emissions are mainly due to the decarbonation of limestone for the production of quicklime, the use of lime-pozzolan binders with the least amount of hydrated lime is relevant.

Vitruvius (30-20 B.C.) described Roman building materials using zeolitic tuff and pumices originated from Italy in the Vesuvius area. The term "pozzolan" comes from an Italian city called Pozzuoli and is originally associated to trachytic fall deposits [7]. However, depending on the geological context, other lithologies may be considered as pozzolans. The latter are actually defined as raw materials that are able to provide cementation when combined with lime and water. According to Pichon [8,9], the hardening of lime-pozzolan blends occurs through the dissolution of silica and alumina within the volcanic glassy phase by calcium hydroxide attack. In addition, the vesicular nature of pyroclastic materials contribute to their reactivity [10]. Most of the traditionally used natural pozzolans are of trachytic or rhyolitic composition with a silica content of 60 — 70 wt.% and are reported to present a better reactivity compared to basic and ultrabasic pyroclastics (i.e. basaltic) for which the silica content is under 45 — 50 wt.% [3,7,10]. However, along French lines and more specifically in the French Massif Central, pozzolans only refer to scoria of basaltic composition and are well-known in the field of quarrying. These basaltic pyroclastics are mainly used for winter road sanding, water drainage or road engineering but not in the cement industry [7]. Only a few old research studies about the mixing of these pyroclastics with lime for road applications were published in the 1970s [11,12].

Furthermore, the building sector is also challenged by a growing shortage of non-renewable mineral resources and has to find meaningful alternatives to quarry materials. In addition, natural pozzolans are not locally available in the North of France (Hauts-de-France area) and there is limited access to deposits for environmental reasons. Instead, dredged sediments are abundant in this area, deposited as well in waterways as on the seafloor of coastal ports (e.g. port of Dunkirk). The composition of marine dredged sediments is partly provided by terrigenous sources resulting from physical and chemical weathering of crustal rocks. The main resulting solid products are quartz sand and clay minerals, due to winds and water current flows over lands composed of sandstone, mudstone, etc. Since quartz is the most stable form of silica in the earth's crust, this mineral is often predominant [13]. Marine sediments can also contain biogenic deposits in the form of calcite in addition to alumino-silicates. Although pozzolanic reactivity is regularly assigned to the glass content of materials, the ability of some mineral components to bind lime was found to be non-negligible [14]. Some authors showed a subsequent pozzolanic reactivity of crystallized quartz after an accurate micronization and a curing temperature of 100°C [15]. Thus, they defined a critical median diameter of 5 micrometers below which quartz particles show an interesting reactivity. Moreover, Diamond et al. [16] investigated the reactivity and the hardening of mixtures with 30 wt.% of lime and 70 wt.% of pure quartz or clays (kaolinite and montmorillonite). The blends were stored under endogenous conditions for 55 days at 60°C. In these specific curing conditions, calcium hydroxide was consumed and the reaction products were C-S-H but also calcium aluminate hydrates in the case of lime-clay blends, especially hydrogarnet

(C_3AH_6). Hence, these results lead one to believe that cementation of mixtures made out of marine sediments and hydrated lime could occur.

The objective of this paper is to provide a new insight into the development of lime-pozzolan binders using marine dredged sediment as reactive powder in combination with hydrated lime. The marine dredged sediment will be used without any thermal treatment (i.e. calcination) but following micronization by air jet milling. In some previous investigations, sediments were used only as supplementary cementitious materials (SCMs) in the field of waste recovery in cement binders. Conversely, several studies about lime-pozzolan binders revealed that the optimal lime content to achieve the best strength performances was in the range of 15 to 30 wt.% [3,7,8,11,17–19]. Hence, this is an opportunity to include a substantial amount of marine sediment in the mix design. The marine dredged sediment that will be used herein is from the port of Dunkirk in the North of France. It will be related to basaltic pyroclastic deposits from the Devès plateau in the French Massif Central. Following mechanical treatment (micronization or grinding), the raw materials will be mixed with 20 wt.% of hydrated lime. The pozzolanic reactivity should be claimed if the different variables of the function in Eq. 1 follow on from each other. Therefore, this paper deals with an evaluation of reaction kinetics, reaction products, microstructure, porosity and compressive strength development until 180 days.

Pozzolanic reactivity = f (Fixed Lime → Reaction products → Porosity → Hardening) (1)

Since high curing temperature is known to significantly increase the pozzolanic reaction rate due to accelerated reaction kinetics following the Arrhenius law [20,21], two curing temperatures will be considered i.e. 20°C and 50°C.

2. Materials and methods

2.1. Raw materials

2.1.1. Pyroclastic deposits

Weakly consolidated basaltic pyroclastic deposits (tephras) were collected in the Devès basaltic plateau (French Massif Central) in 2019. The geological context of this environment is linked to Strombolian eruptions of the Pleistocene time (~ 2.5 Ma) [22]. Lava flows occur simultaneously with incandescent ejections that undergo a sudden cooling in the atmosphere. The pyroclastic fall deposits (i.e. bombs, lapilli and cinders) build up around the vent to form the volcanic edifice. Almost 150 scoria cones are counted over this basaltic plateau (Fig. 1a). Samples were taken from different sites in the middle part of the plateau (see the different geographic locations on the map of Fig. 1a). Fig. 1b shows one of the quarry faces. The pyroclastics used in this investigation (thereafter noted SDA, MTB, COS and BZ depending on the site) were composed of highly vesiculated lapilli-size millimetric fragments (Fig. 1c).

2.1.2. Marine dredged sediment

The marine sediment (thereafter noted MS) was dredged in the port of Dunkirk (North of France) in 2019 and stems from an active lagooning process (Fig. 1d). The fines content of the raw sediment (illustrated in Fig. 1e) was determined by wet sieving at 63 micrometers and was 40 wt.%. The particle size distribution of clay and silt grades by laser diffraction is reported in Fig. 2a. For the sand fraction, it was performed by mechanical sieving and the result is shown in Fig. 2b. The marine sediment can be considered non-hazardous and non-inert based on heavy metals and organic contents in eluates in accordance with criteria and procedure for waste acceptance at landfills (99/31/EC).

2.1.3. Hydrated lime

A commercial hydrated lime (SuperCalco®97 from Carmeuse) with 94 wt.% of calcium hydroxide ($Ca(OH)_2$) and 1.2 wt.% of calcite ($CaCO_3$) was employed.

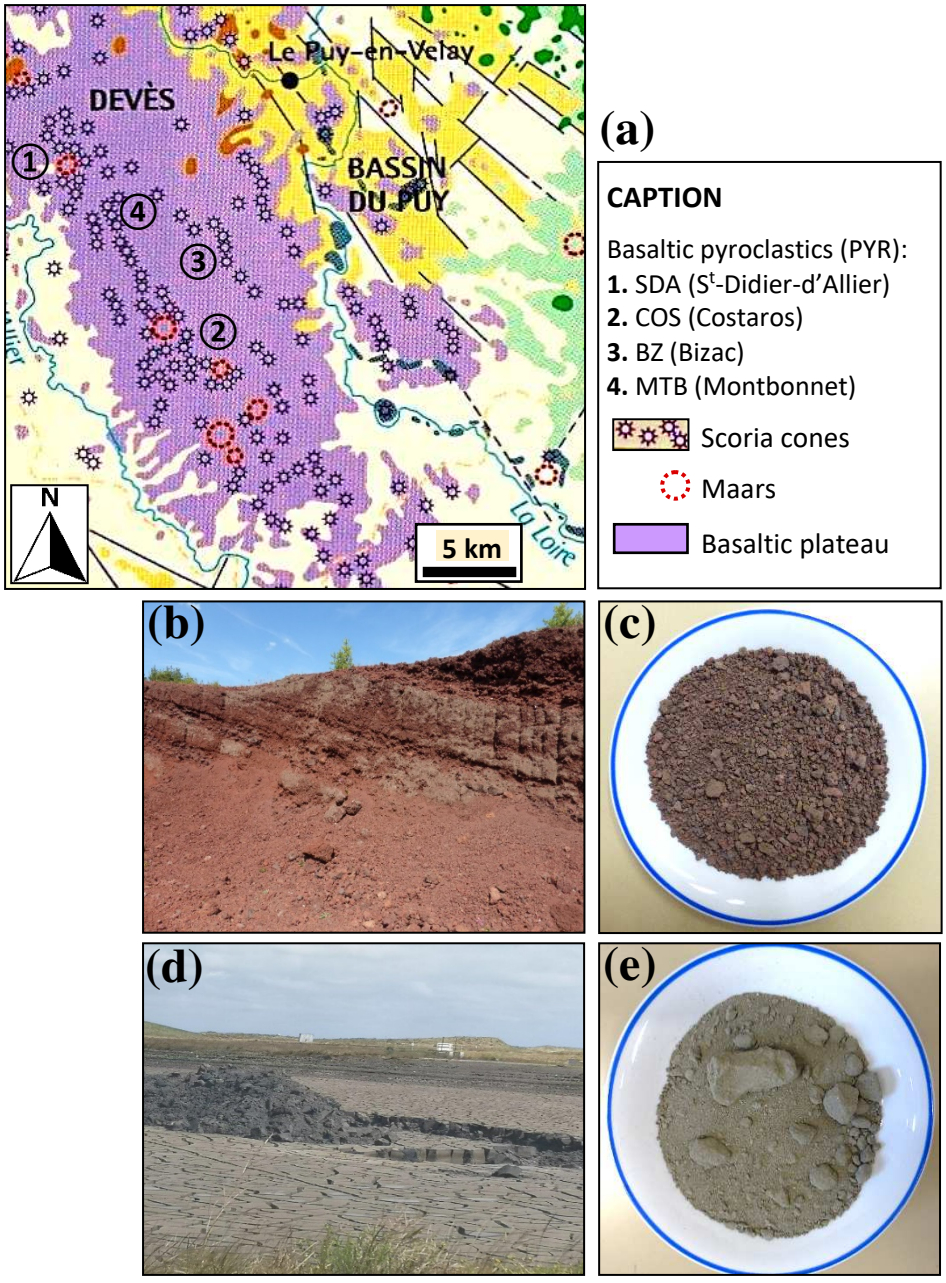

Fig. 1. (a). Geological map of the Devès plateau [22], **(b)** Quarry face, **(c)** Pyroclastics in the form of millimetric aggregates (lapilli), **(d)** In-situ dehydration of the marine sediment after dredging, **(e)** Raw marine dredged sediment

2.2. Experimental methods

2.2.1. Preparation of materials

Following receipt in the laboratory, the raw materials (pyroclatics and marine dredged sediment) were dried at 50°C. The pyroclastics were ground using a cross beater mill (maximum diameter of 250 micrometers) followed by a more intensive grinding with a vibratory disc mill at 700 rpm for 5 minutes. The marine dredged sediment was ground using a rotor beater mill (maximum diameter of 500 micrometers) with a speed of 10,000 rpm in order to get the suitable maximum particle size for the use of air jet milling. The equipment was set up to micronize the sediment powder at a median diameter (D_{50}) of 2.3 micrometers.

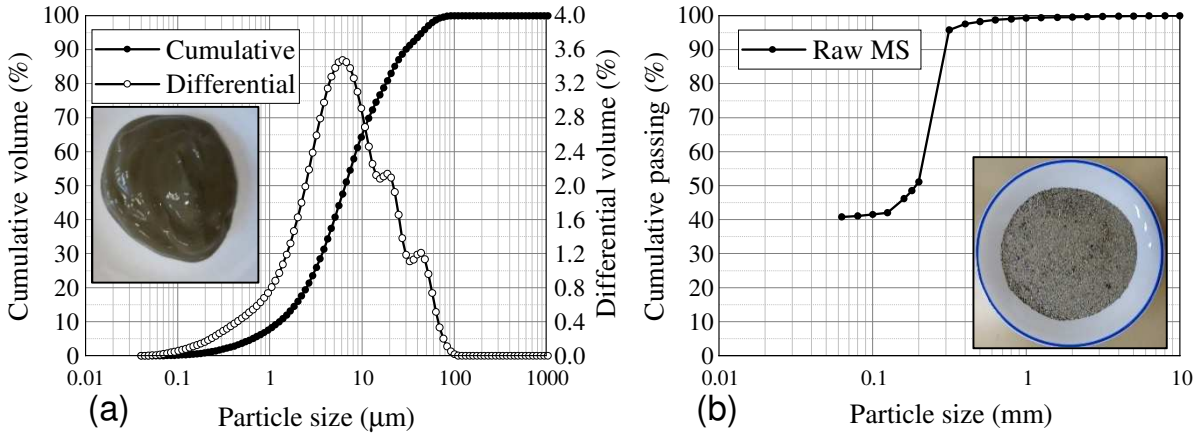

Fig. 2. Size distribution of **(a)** wet-sieved particles under 63 µm, **(b)** sand fraction over 63 µm for the raw marine dredged sediment

2.2.2. Mix design and curing conditions

Based on past experiences with regard to lime-pozzolan blends [3,7,8,11,17–19], the pastes studied in this paper were made up of 80 wt.% of ground pyroclastics or micronized sediment mixed with 20 wt.% of hydrated lime. The water-on-powder mass ratio (W/P) of the pastes combining each of the materials with hydrated lime were determined using a flow spread test [23]. The mixtures were cast into cylindrical molds (2.7 cm in diameter and 5.4 cm in height) under the effect of vibration and the molds were placed in hermetically sealed vials to ensure endogenous conditions (RH higher than 95%) and avoid carbonation of hydrated lime for the curing time. Immediately after casting and sealing, samples were cured either under standard moist curing at room temperature (20°C) or under elevated temperature (50°C).

2.2.3. Compressive strength test

The tests were conducted on the cylindrical specimens with an electromechanical standard press (Instron). A load cell of 10 kN was used to provide a suitable accuracy for low strength materials and the loading rate was 1.5 $kN.min^{-1}$. The compressive strength was tested from 3 to 180 days. For each testing age, samples were polished and the strength reported is an average of 3 to 5 specimens. Although kneading water plays a significant role in strength loss during early ages [24], the samples were tested with their water saturation degree since drying of pastes would result in shrinkage cracks, especially when the hydration degree is high.

2.2.4. Method for hydration stoppage

The characterization of reaction kinetics, reaction products, microstructure, and porosity after a given degree of reaction require the removal of capillary water while preserving at the most the physical and chemical state of the samples [25,26]. As such, a drying method by solvent exchange with IPA (Isopropyl alcohol or 2-propanol) was used. A representative sample of the cylinders was reduced to powder for TGA and XRD analyses and immersed in IPA for 7 days. IPA was renewed twice (each time for 48 hours) to facilitate the diffusion process. In the end, IPA was evacuated by a vacuum filtration process and completely removed by vacuum drying until constant mass, using a desiccator with silica gel and hydrated lime. Samples were actually kept under vacuum until analysis to avoid carbonation as far as possible. The same protocol was followed for little cubic samples that were carefully cut from cylinders for MIP and SEM.

2.2.5. Bound water and fixed lime by TGA

TGA (Mettler Toledo) was performed under nitrogen atmosphere from 25°C to 950°C with a heating rate of $10°C.min^{-1}$. Chemically bound water in hydrates was estimated from mass loss in

the range 80°C – 400°C [27]. Free lime (CH) and calcium carbonate (CC) were quantified by the tangential method [28] respectively in the range 400 – 500°C and 500°C – 800°C using the following equations (Eq. 2&3):

$$\text{Free CH (\%)} = \text{WL}_{\text{CH}}\ (\%) \times \frac{\text{m(CH)}}{\text{m(H}_2\text{O)}} \quad (2)$$

$$\text{CC (\%)} = \text{WL}_{\text{CC}}\ (\%) \times \frac{\text{m(CC)}}{\text{m(CO}_2\text{)}} \quad (3)$$

where WL_{CH} and WL_{CC} are respectively the weight losses due to dehydroxylation of CH and decarbonation of CC with a normalization to the anhydrous binder and m is the molecular mass of CH (74 $g.mol^{-1}$), H_2O (18 $g.mol^{-1}$), CC (100 $g.mol^{-1}$) and CO_2 (44 $g.mol^{-1}$).

The amount of fixed CH by the pyroclastics or the sediment over time (until 180 days of curing) was calculated as percent of the initially available CH as follows (Eq. 4):

$$\text{Fixed CH (\%)} = [(\text{CH}_i\ (\%) - \text{Free CH (\%)} - \text{Carbonated CH (\%)})/\text{CH}_i\ (\%)] \times 100 \quad (4)$$

where CH_i (%) is the amount of CH initially introduced into the blend and carbonated CH (%) is the free lime that underwent carbonation.

2.2.6. Reaction products (DTG, XRD) and microstructure (SEM-EDS)

Analysis of newly formed phases was done using DTG curves and XRD (Bruker D2 phaser) with Cu Kα radiation, 2θ from 10 to 80° and step size of 0.02°.
The microstructure of pastes after 90 days of hardening was investigated using Scanning Electron Microscopy (SEM Schottky emission Hitachi, Model S-4300Se/N). Prior to observations, cubic samples need to be embedded in epoxy resin, polished and coated with a carbon film.
Images were acquired in backscattered electron imaging mode (BSE) and the acceleration voltage was 20 kV. Semi-quantitative chemical analysis was also performed by means of Energy Dispersive X-ray Spectroscopy (EDS Silicon drift detector, Thermo Electron Corporation) coupled with SEM with the aim of studying the composition of hydrated phases (Ca, Si, Al). Elemental compositions were recorded for 60 seconds live time at 20% dead time.

2.2.7. Porosity (MIP)

The samples were subjected to porosity measurement after 90 and 180 days of hardening. The equipment was an AutoPore V 9600 Mercury porosimeter (from Micromeritics). Paste samples were inserted in a penetrometer for solids with a cup volume of 5 cm^3 (and capillary tube of 1.8 cm^3). The measurement included one intrusion-extrusion cycle and was carried out until maximal pressure of 200 MPa, corresponding to a minimal pore radius of about 6 nm. The step mode was used for the increase in pressure and the equilibrium time between each pressure increment was 20 seconds. The surface tension of mercury is 0.485 $N.m^{-1}$ and its contact angle with the sample was 130°.
The curve of cumulative pore volume was plotted from the volume of intruded mercury under pressure and gives the total volume of connected pores in the whole sample. Then, the differential intrusion distribution was calculated from the cumulative mercury intrusion. With these two curves illustrated in Fig. 3, it was possible to examine the pore size distribution, the critical pore diameter which corresponds to the recorded diameter for the maximum value of differential intrusion, and the median pore diameter calculated at 50% of cumulative pore volume [29].

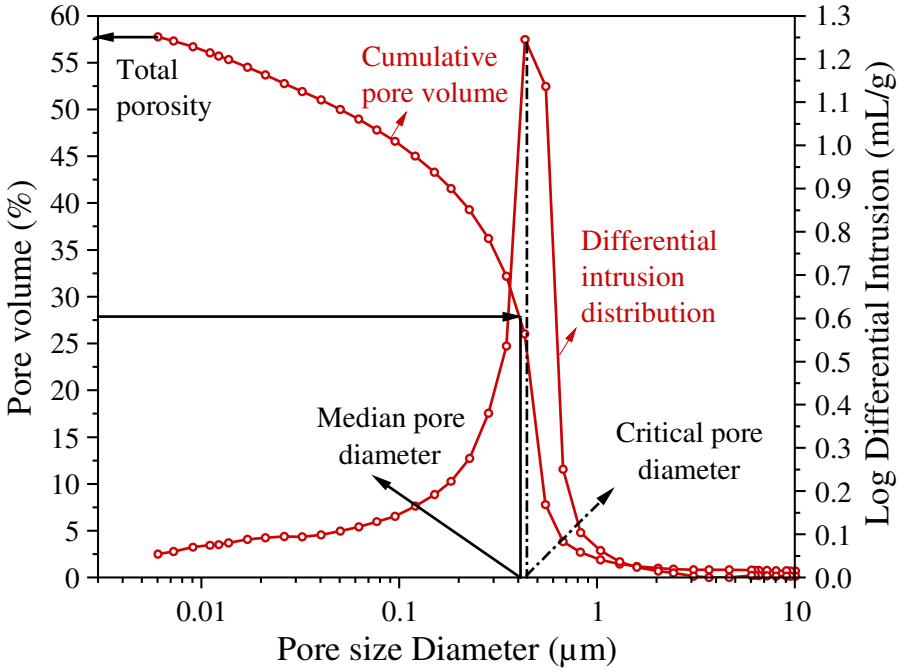

Fig. 3. Typical cumulative and derivative MIP curves for the lime-sediment binder. Adapted from Berodier et al. [30]

3. Results and discussion

3.1. Characterization of materials

3.1.1. Chemical and mineralogical composition

The chemical compositions of pyroclastics are presented in Table 1 and are representative of basaltic or basanite deposits from the alkaline series according to the Total Alkali-Silica (TAS) diagram (Fig. 4) [31]. The pyroclastics were silica-undersaturated (SiO_2 content of 41 – 45 wt.%) with 3.5 – 6 wt.% of Na-K feldspars and their Al_2O_3 and Fe_2O_3 contents were relatively close together. The XRD patterns of pyroclastics are reported in Fig. 5. The main mineralogical phase was augite (monoclinic pyroxene) as well as plagioclase feldspars (anorthite or labradorite) and forsteritic olivine. Alkali basalts never contains free silica (quartz) since the latter is not consistent with the presence of olivine. However, nepheline (feldspathoid, $Na_3KAl_4Si_4O_{16}$) was clearly identified for BZ and COS, linked to their higher alkali content (~ 6 wt.%) compared to other pyroclastics. In addition, analcime ($NaAl(Si_2O_6),H_2O$) was only detected for SDA. This mineral belongs to the family of zeolites but is also very close to some feldspathoids and quite common in silica-undersaturated basaltic materials. The presence of hematite (accessory mineral) is linked to iron oxide providing the red colour.

Table 1. Chemical composition of materials (previously calcined at 550°C) by XRF (in wt.%)

Materials	SiO_2	Al_2O_3	Fe_2O_3	CaO	MgO	Na_2O	K_2O	TiO_2	P_2O_5	MnO	SO_3	LOI
SDA	44.7	13.6	11.8	10.5	11.3	3.2	0.6	2.6	0.6	0.2	–	0.34
MTB	41.0	12.1	12.4	10.7	11.6	2.1	1.4	2.6	0.5	0.2	–	4.8
COS	44.5	13.8	11.3	9.4	8.9	4.4	1.6	2.5	0.6	0.2	–	2.4
BZ	44.8	13.2	11.5	8.5	9.3	4.2	1.5	2.2	0.6	0.2	–	3.4
MS	73.4	3.0	1.9	8.3	0.5	1.0	0.9	0.1	0.1	–	1.1	9.3

XRD patterns have not shown a clearly visible amorphous halo, suggesting a low content of uncrystallized volcanic glass, as was evidenced in literature with around 5% of vitreous phase in basaltic pyroclastics of same origin (Devès) [32]. Nevertheless, some authors [33 – 35] argue that feldspars could be involved in the pozzolanic reaction. According to Dron and Brivot [35], the

glass content of pozzolans that contain a high proportion of calcium-rich feldspars (i.e. anorthite) is likely to be low. Hence, the authors suggest to calculate the difference SiO_2 – CaO (wt.%) with a threshold around 34% under which the glassy phase is not present. For the pyroclastics studied in this work, this difference is in the range 34 – 36 %, with the exception of MTB (~ 30%).

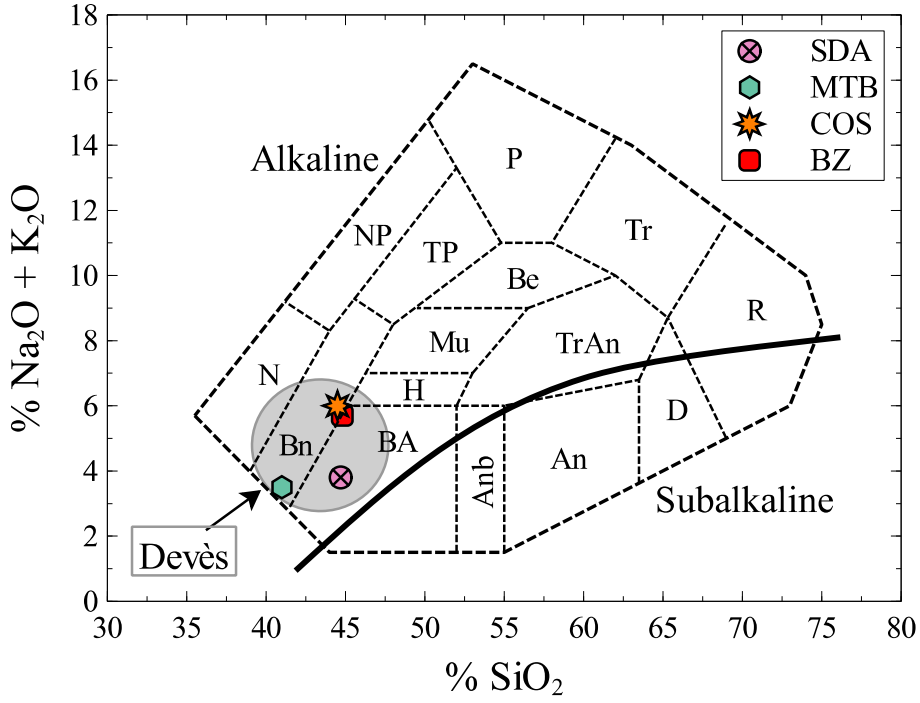

Fig. 4. Total Alkali-Silica (TAS) diagram. (N: Nephelinite, NP: Nephelinite - Phonolite, P: Phonolite, Bn: Basanite, BA: Basalt, TP: Tephrite - Phonolite, Be: Benmoreite, Mu: Mugearite, H: Hawaiite, An: Andesite, Anb: Andesite - Basalt, Tr: Trachyte, TrAn: Trachyandesite, D: Dacite, R: Rhyolite) [31]

The oxide composition of the sediment following micronization is reported in Table 1. It shows a very high content of SiO_2 (73%) compared to pyroclastics. This is due to the predominance of quartz sand. In contrast, it can be observed a poor amount of aluminum, iron, and magnesium oxides. These XRF results are consistent with the XRD pattern (Fig. 6) where the presence of quartz is significant whereas clay minerals are more difficult to track. However, albite (plagioclase feldspar), gypsum, and calcite were detected. The amount of calcium carbonate was calculated to be 19 wt.% by TGA.

3.1.2. Physical properties

The particle size distribution of the sediment compared to pyroclastics following micronization and grinding processes is shown in Fig. 7. It is interesting to see that the size range of SDA and MTB was the same and their median diameter (noted D_{50} in Table 2) was similar (5 – 5.5 µm). However, COS and BZ exhibited coarser particles, especially BZ for which the median diameter was about 55 µm. The other physical properties are also reported in Table 2. The BET specific surface area showed the highest values for the finest pyroclastics (SDA and MTB). The true density was found to be very close to that of basalt (~ 3 $g.cm^{-3}$) and LOI at 550°C was in the range 0.35 – 1.61%, except for MTB for which it was less than 4%.

It can be observed a higher BET specific surface area for SDA and MTB compared to the marine sediment. In view of the particle size distribution illustrated in Fig. 7 and median diameters (Table 2), this result is probably due to the porosity within powdered grains of pyroclastics. Indeed, the BET method is especially valuable for revealing the large internal pore structure of these vesicular materials. The true density of the sediment (2.65 $g.cm^{-3}$) was close to that of sand and LOI at 550°C was 5% (Table 2).

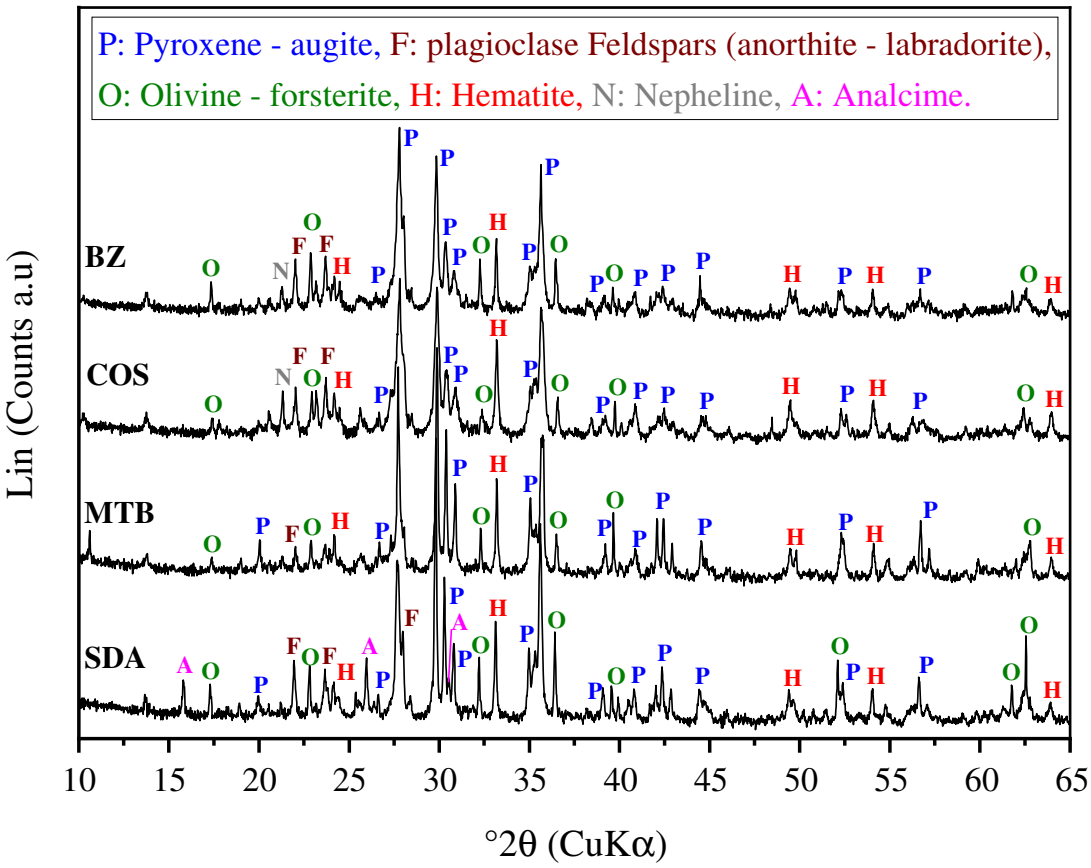

Fig. 5. XRD patterns of pyroclastics

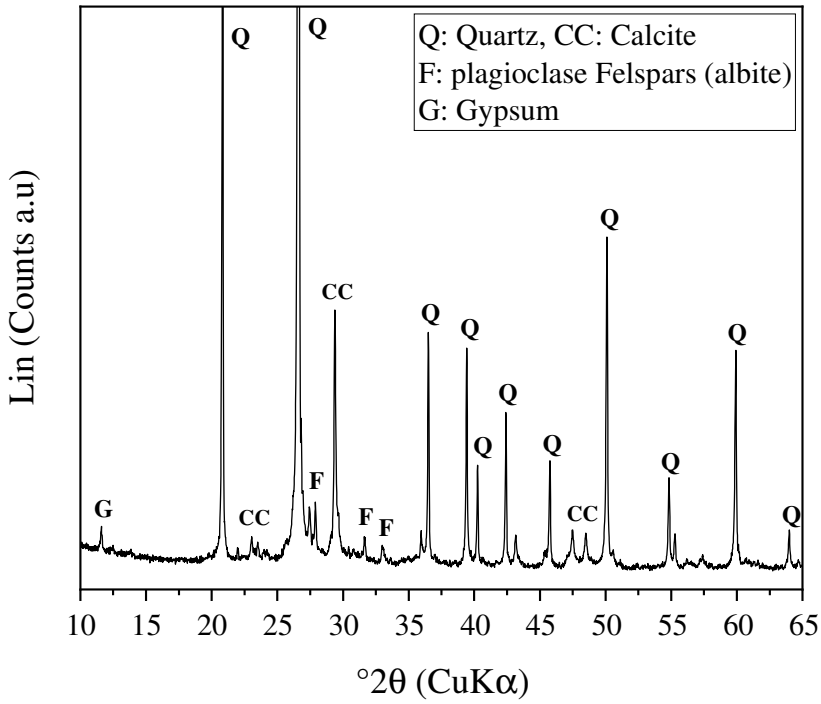

Fig. 6. XRD pattern of the marine dredged sediment

Fig. 7 also presents the particle size distribution of hydrated lime. It can be seen that its size range is similar to that of the micronized marine sediment up to 2.5 micrometers but the maximum size diameter of hydrated lime was around 12 micrometers. In addition, the huge BET specific surface area of hydrated lime should be noted (less than 18 $m^2.g^{-1}$, see Table 2).

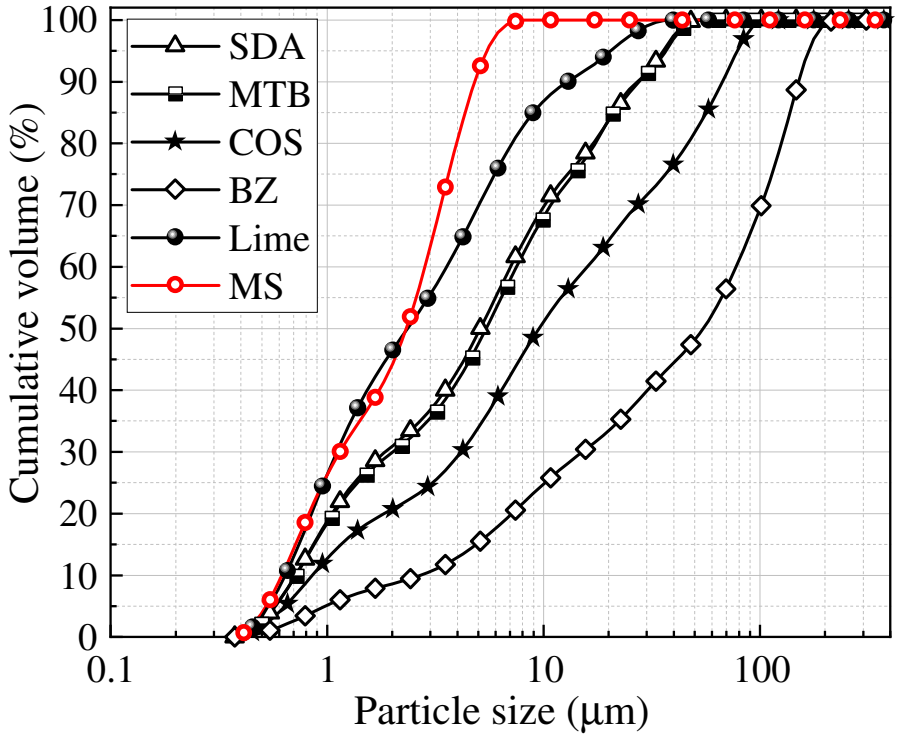

Fig. 7. Particle size distribution of powders after grinding processes

Table 2. Physical properties of ground pyroclastics, micronized sediment and hydrated lime

Materials	SDA	MTB	COS	BZ	MS	Lime
D_{50} (µm)	5.11	5.44	9.65	54.78	2.32	2.36
BET-SSA ($m^2.g^{-1}$)	6.06	9.67	2.46	1.07	4.54	17.66
True density ($g.cm^{-3}$)	3.06	3.05	3.09	3.01	2.65	2.33
LOI – 550°C (wt.%)	1.61	3.73	0.47	0.35	4.99	–

Related to these physico-chemical properties, the water-on-powder mass ratios (W/P) of pastes determined from the flow spread test are reported in Table 3. As expected, the water demand was strongly linked to particle size distribution and specific surface area of powders.
The wet bulk density of hardened pastes was around 1.8 for lime-pyroclastics pastes (L–PYR) and around 1.55 for the lime-sediment paste (L–MS). The specimens are pictured in Fig. 8. It should be noted that blends of lime and SDA will be named L–SDA and the same designation will be used for other pyroclastics.

Table 3. Water demand of pastes (W/P ratio)

Blends	L–SDA	L–MTB	L–COS	L–BZ	L–MS
W/P (80 PYR or MS + 20 L) wt.%	0.46	0.49	0.42	0.38	0.73

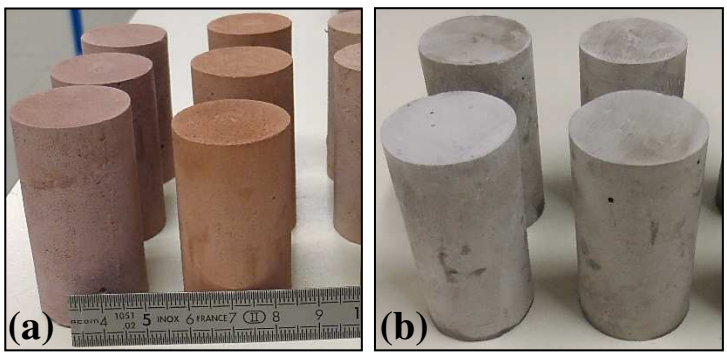

Fig. 8. Cylindrical specimens **(a)** L–PYR or **(b)** L–MS

3.2. Compressive strength development

The compressive strength development of pastes is reported in Fig. 9a for room temperature (20°C) and Fig. 9b for elevated temperature (50°C). At 20°C, L—MTB did not harden until 180 days. On the opposite, a compressive strength of 4.7 MPa was reached for L—SDA after 180 days. The L—MS paste was able to show an initial hardening from 90 days and finally reached 0.8 MPa after 180 days. The absence of hardening at 20°C within a reasonable time shows that an increase of curing temperature is needed. It should be noted that blends including lime and natural pozzolans often require high temperature (38°C in the work of Pichon [8]) or chemical activators [17] to achieve a suitable hardening.

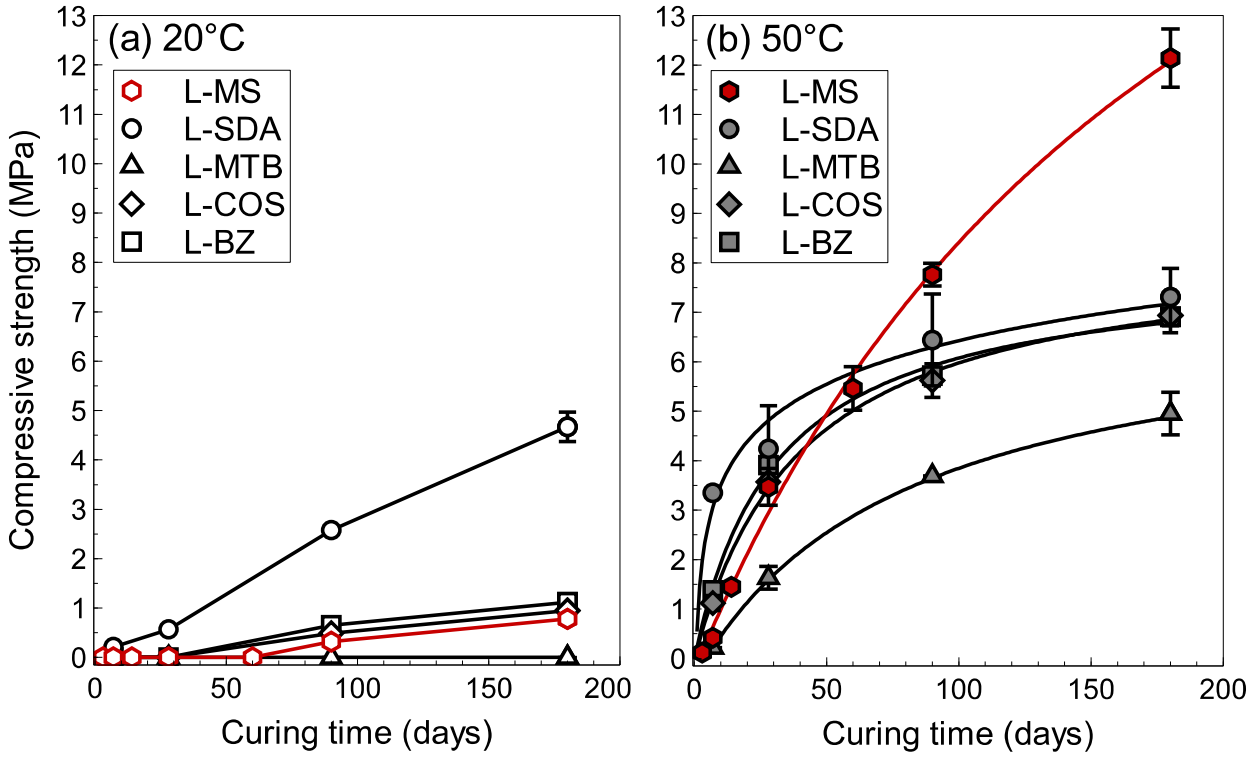

Fig. 9. Compressive strength development of pastes over time depending on the curing temperature **(a)** 20°C, **(b)** 50°C

Strength results at 50°C were markedly different. Regarding the pyroclastics for which the hardening of pastes at 20°C was low or non-existent (MTB, BZ, and COS), the rise in curing temperature has obviously resulted in a higher compressive strength from 7 to 180 days. The compressive strength of L—MTB was 5 MPa after 180 days while the paste did not show measurable strength at this date for a curing at 20°C. It is interesting to note the same strength development for the pastes designed with COS and BZ. Those pyroclastics were very different in terms of size distribution (see Fig. 7) but their specific surface area was quite similar compared to SDA and MTB. Moreover, the chemical composition of COS and BZ was almost identical as shown in the TAS diagram (Fig. 4). Ultimately, the compressive strength at 180 days was in the range 6.9 – 7.3 MPa for the pastes with BZ, COS and SDA. For the most reactive pyroclastic material from a mechanical point of view (i.e. SDA), it can be seen that the rise in curing temperature accelerated the early age strength (3.3 MPa at 50°C versus 0.2 MPa at 20°C after 7 days). However, since the strength tended to level off after 90 days, the compressive strength after 180 days at 50°C (7.3 MPa) was not so far from that reached at 20°C (4.7 MPa).

The measurable strength of L—MS at 50°C was extremely low until 7 days and it was 1.45 MPa after 14 days. This is partly explained by the high water-on-powder mass ratio used for this blend (0.73) compared to the others. However, the strength development of L—MS at 50°C beyond 7 days was of great significance. It is readily seen that the effect of curing temperature became

increasingly remarkable with time. After 90 days, the compressive strength of L–MS exceeded those achieved with L–PYR. From 90 days to 180 days, the compressive strength of L–MS kept going up to reach 12.1 MPa. The gap between this performance and the compressive strength recorded at 20°C (0.8 MPa) shows that the apparent activation energy of the micronized marine sediment is very high.

3.3. Reaction kinetics

The amount of fixed CH by the studied materials as percent of the initially available CH is illustrated in Fig. 10a for 20°C and Fig. 10b for 50°C.

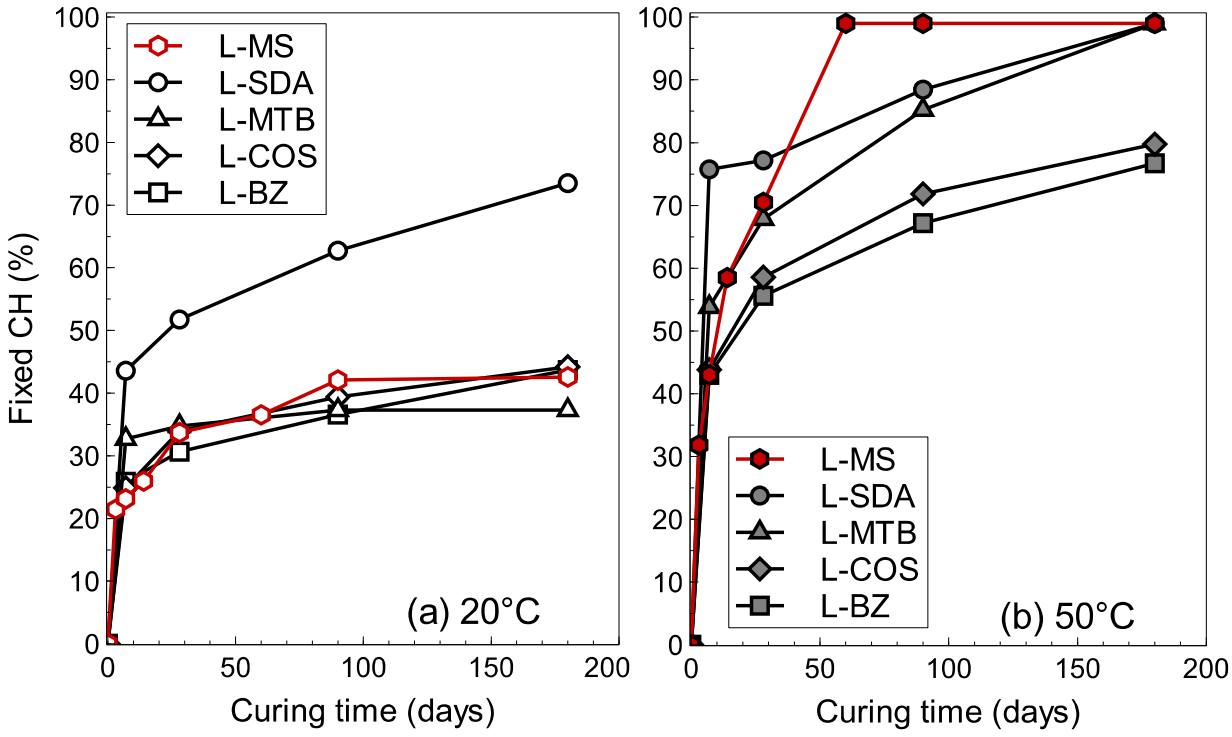

Fig. 10. Evolution of fixed CH over time depending on the curing temperature **(a)** 20°C, **(b)** 50°C

For both curing temperatures, CH was consumed very quickly during the first days and much more slowly thereafter. This trend is consistent with literature regarding especially natural pozzolans [19,21,27,36,37]. The initial reaction rate of natural pozzolans can be higher than that of some fly ashes and with time, the reverse trend occurs [38]. This was attributed to their higher specific surface area giving a high initial rate of lime combination [39]. At 20°C, this combination rate was noted to be low from 28 days (or even 7 days) to 180 days and after six months of curing, the percentage of fixed CH did not exceed 45%, except for L–SDA. However, at 50°C, the combination rate increased at the early age and until 180 days. For L–BZ and L–COS, the amount of fixed CH after 180 days at 50°C was less than 80%, namely twice the rate reached at 20°C. This result is even stronger with L–MS for which the combination rate at 50°C was very significant from 3 days to 60 days, rising from 32% to the whole content of initially available CH. This observation obviously highlights the effect of curing temperature on the reaction rate.

In the study of Millet and Hommey [12], the reactivity of some basaltic pyroclastics was found to be very low at 20°C and a chemical equilibrium was reached only after one year. In their work, Diamond et al. [16] also found a considerable amount of unreacted CH after a long reaction period of 6 months between lime and clay at 23°C whereas most of the CH had disappeared for a curing at 60°C with clay and pure quartz. In the case of SDA, the combination rate at 20°C was

higher than those recorded for the other pyroclastics. It can be seen that the percentage of fixed CH, especially in the long term, is well correlated with the compressive strength development. SDA was the only one able to fix more than 70% of CH after 180 days at 20°C. In addition, the amount of fixed CH after 7 days was clearly improved at 50°C (more than 75% versus less than 45% at 20°C).

More generally speaking, for a given curing temperature, the rate of lime combination is reported to be strongly linked to the specific surface area of pozzolanic materials and to the water-on-powder mass ratio [21]. Hence, at 50°C, it is interesting to note that higher amounts of fixed lime were calculated for pyroclastics exhibiting the higher specific surface area i.e. MTB (9.7 $m^2.g^{-1}$) and SDA (about 6 $m^2.g^{-1}$). Overall, at 50°C, CH combination was found to be strongly correlated with the specific surface area of ground pyroclastics. However, it must be noted that MTB should be able to fix more CH than SDA due to its very high specific surface area (and the higher W/P) but this was not the case at 20°C. Since the long-term activity is more related to the nature and the content of reactive phases [21,40], MTB could present a deficiency in these phases or include some harmful components (see LOI in Table 2) due to potential alteration [41].

The strength development of lime-pozzolan binders is not only dependent on the amount of fixed lime but also, and above all on the type of hydration products. As a matter of fact, while the sediment was able to fix 34% of lime after 28 days at 20°C, this has not resulted in a suitable hardening of the paste. From there, it is interesting to study the chemically bound water in hydrates over the curing time as illustrated in Fig. 11a for 50°C.

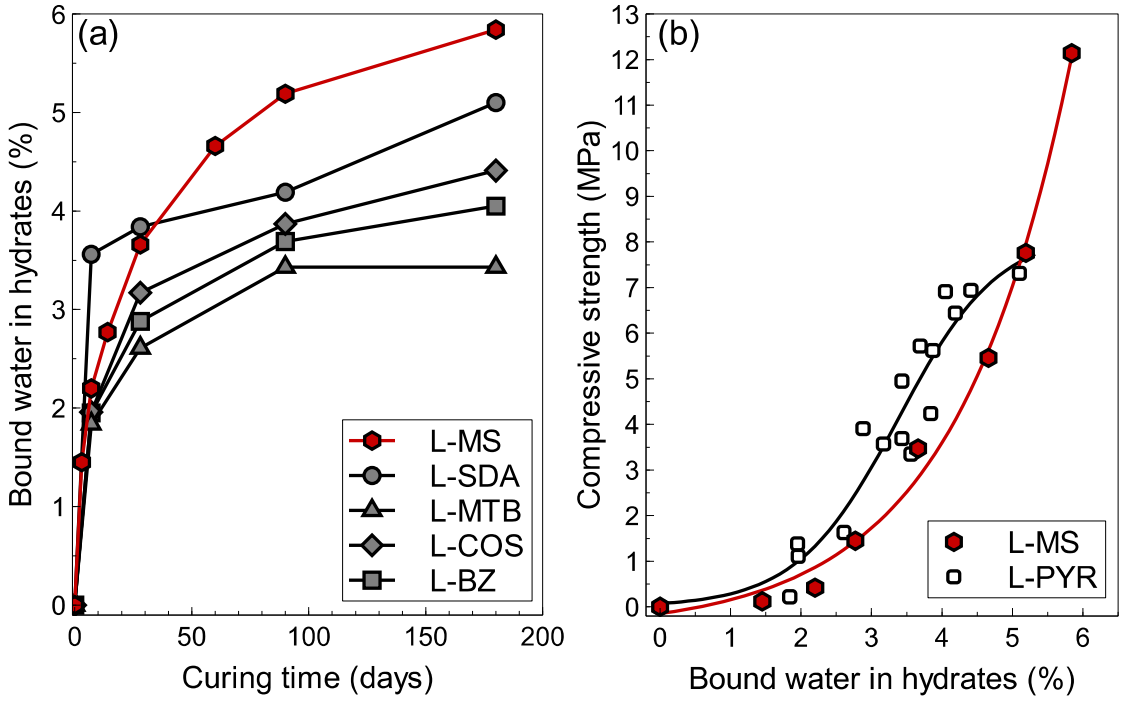

Fig. 11. (a) Evolution of bound water in hydrates over time at 50°C, **(b)** Relationship between bound water and compressive strength at 50°C

A very good correlation was found between the combination of CH and bound water. The highest amount of bound water over time was reported for L—MS and L—SDA. It is also noted that L—BZ and L—COS were very close to each other as was the case for fixed CH and compressive strength development. The only exception was L—MTB for which the amount of bound water was the lowest whereas the percentage of fixed lime after 180 days of curing was 100% as well as for L—SDA and L—MS (Fig. 10b). The ratio of bound water to fixed CH was in the range 0.27 – 0.28 for L—SDA, L—COS and L—BZ, 0.31 for L—MS and only 0.19 for L-MTB. Even if MTB was

able to fix all the CH due to its huge specific surface area, the resulting reaction product assemblage was probably affected [42]. Fig. 11b reports the relationship between compressive strength and bound water. For the pyroclastics, the S-shape of the curve fitting all the points was also found by Fournier and Geoffray [11]. The same trend was observed for the marine sediment but the stabilization did not occur within the allotted time. For all materials, the results suggest that the reaction products formed at the early age exhibit poor binding properties and this could be related to their Ca/Si ratio or their small size leading to insufficient interconnection as is also the case at 20°C. High curing temperature is needed for CH to be sufficiently depleted giving rise to hydrates further contributing to the strength over a lengthy period of time, as suggested in some research works [42–44]. Since the water content of hydration products (C-S-H) is expected to decrease with hydration time [38], this could explain the slope of the curve that becomes increasingly important.

3.4. Reaction products and microstructure

3.4.1. TGA-XRD

Newly-formed hydrated phases were identified by means of DTG curves illustrated in Fig. 12 and XRD patterns reported in Fig. 13. The results are presented after 90 days of curing.

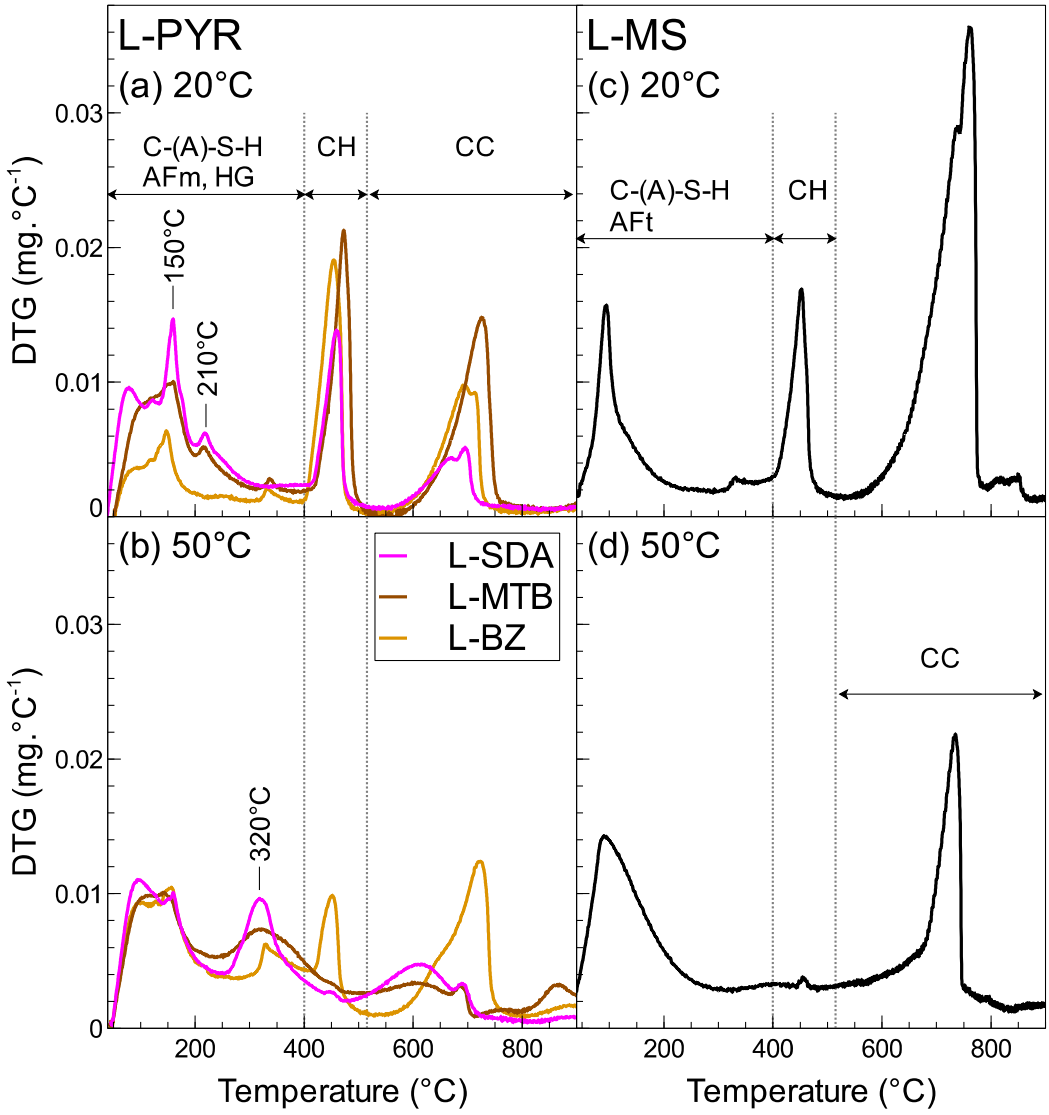

Fig. 12. DTG curves after 90 days of curing **(a)** L–PYR at 20°C, **(b)** at 50°C, **(c)** L–MS at 20°C, **(d)** at 50°C. Note: L–COS is not reported since the signal was identical to L–BZ.

In the case of L─MS, the single mass loss up to about 240°C (Fig. 12) is due to the dehydration of C-S-H and C-A-S-H (i.e. C-S-H with the inclusion of Aluminum) [45]. C-S-H could not be detected by XRD due to an important overlapping with the diffraction peak of calcite (CC in Fig. 13b). However, at 20°C, AFt (ettringite, $C_6As_3H_{32}$) was found as a new phase by XRD (Fig. 13b). This is consistent with the disappearance of gypsum that was present in the marine sediment. At 50°C, AFt was present after 28 days but not after 90 days (see Fig. 13b) suggesting that it was destabilized. In view of the very low SO_3 content in the sediment (Table 1), AFt should transform into AFm quickly [46] but this could not be shown conclusively herein. Beyond this, the alumina content of the sediment was also low compared to that of the pyroclastics (3% versus 12-14%) thus justifying the absence of calcium aluminate hydrates. On another note, the absence of CH on the XRD pattern at 90 days is consistent with the whole combination of initially available CH after 60 days of curing at 50°C (Fig. 10b). Furthermore, XRD results show that albite was apparently involved in the pozzolanic reaction since the diffraction peak for $2\theta = 31.6°$ has disappeared for both curing temperatures by comparison with the raw material.

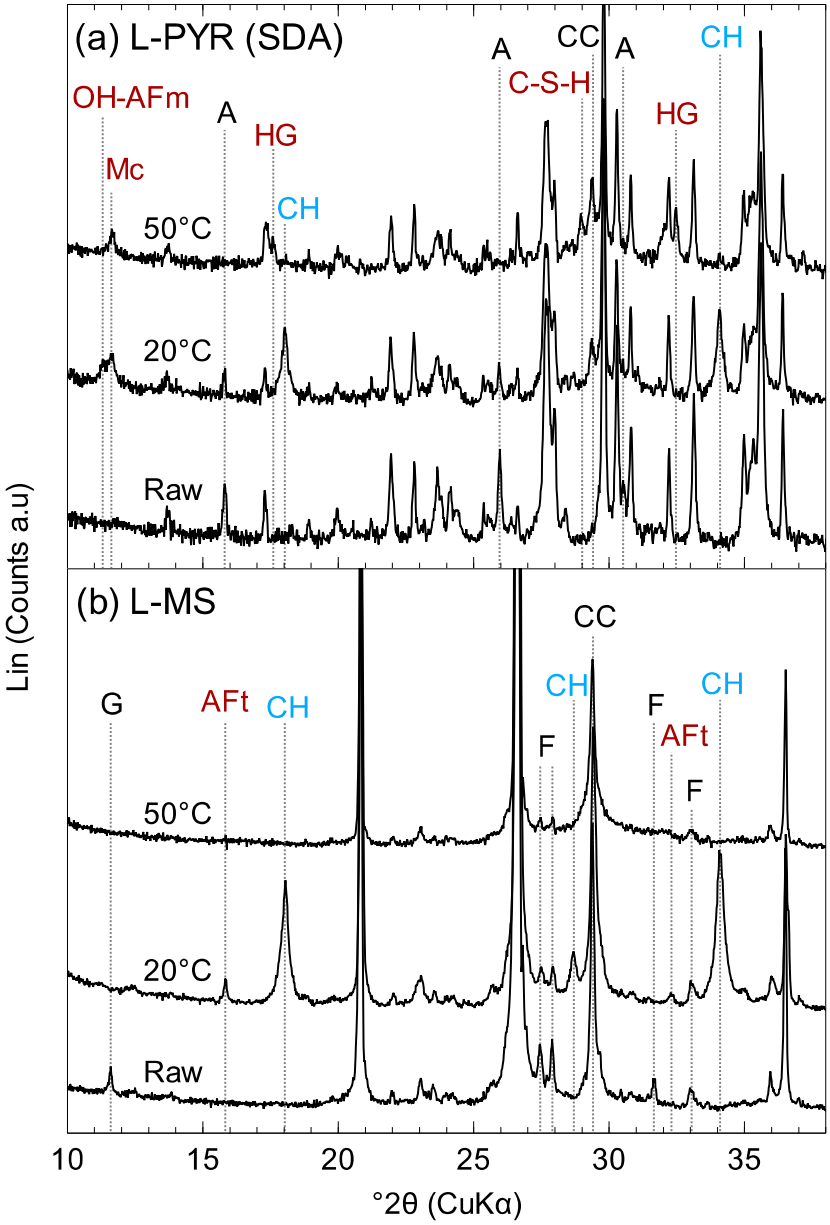

Fig. 13. XRD patterns after 90 days of curing at 20°C or 50°C.
(a) L─PYR, **(b)** L─MS. OH-AFm: Hydroxy-AFm (C_4AH_{13}), Mc: Monocarboaluminate, HG: Hydrogarnet, A: Analcime, G: Gypsum, F: Feldspar – Albite

In the case of L—PYR, a peak at 2θ = 29° revealing the presence of C-S-H was clearly identified for all pyroclastics but only at 50°C (Fig. 13a). The two DTG peaks noted at 150°C and 210°C in Fig. 12a are attributed to the dehydration of AFm phases. The diffraction peaks of C_4AH_{11} and monocarboaluminate (carbonated form C_4AcH_{11}) are very close together [12]. However, due to the presence of CC and according to literature, the presence of monocarboaluminate (Mc) is advanced [8,10,47,48]. The presence of Mc (TG mass loss around 150°C and XRD peak for 2θ = 11.6°) was found for all pyroclastics, both curing temperatures and from 7 to 180 days. Matschei et al. [49] have reported the good thermodynamic stability of Mc until 70°C. The DTG peak at 210°C was observed for L—SDA and L—MTB only at 20°C and from 90 days. It is attributed to the dehydration of C_4AH_{13} [50,51] and was confirmed by the presence of a XRD peak for 2θ = 11.2°. At 20°C, C_4AH_{13} can decompose to hydrogarnet (HG) and CH at long term ages [49], this probably explaining the absence of this phase on the DTG signal for L—BZ and L—COS. At 50°C, an important mass loss was detected around 320°C (Fig. 12b). The latter is assigned to hydrogarnet series $C_3AS_xH_{6-2x}$ (C_3AH_6 — $C_3AS_2H_2$) [21,52,53]. HG are typical hydration products formed under hot water curing, especially above 40°C, and originate from the conversion of metastable C_4AH_{13} [10,51,54]. For L—PYR, HG mass loss occurred as of 7 days and was stable until 180 days. HG was also identified by XRD (Fig. 13a). Furthermore, a very interesting result of XRD is the disappearance of the diffraction peak of analcime for L—SDA at 50°C. This mineral is known to present a significant pozzolanic activity [55]. The lime-binding capability of analcime was reported to be intermediate between the glassy phase and the feldspars of trass (a natural pozzolan) [14]. This is consistent with the higher amounts of fixed CH for L—SDA (Fig. 10). In addition, there was a strong decrease in the diffraction peak of nepheline for L—COS and L—BZ cured at 50°C. Accordingly, the involvement of crystalline minerals (analcime, nepheline, and albite) in the pozzolanic activity of the materials studied in this paper was highlighted.

3.4.2. SEM-EDX

BSE-SEM pictures of microstructures after 90 days of hardening are reported in Fig. 14. The first point is the comparison between L—PYR (Fig. 14a) and L—MS (Fig. 14b) at 20°C. In the case of L—MS, a large number of sharp-edged quartz grains (i.e. pure white in the back-scattered mode) were spread across the section. The grain size was clearly lower compared to that of ground pyroclastics due to the micronization of the marine sediment. At 20°C, lime clumps were frequently observed as illustrated in Fig. 14a. However, it was more difficult to identify the C-(A)-S-H phases for this curing temperature. According to Taylor [44], reaction of lime with quartz surface initially gives a lime-rich substance like C-S-H (II) with a Ca/Si ratio from 1.5 to 2. At 20°C, some phases in the interstitial mass displayed high Ca/Si ratios (i.e. more than 2). It is quite likely that an intermixing occured between free CH and C-S-H phases as this phenomenon has been well described in the research of Rossen and Scrivener [56].

However, it was possible to observe the calcium aluminate phases of L—PYR for both curing temperatures. Fig. 14c and Fig. 14d report pictures with calcium aluminate phases at 50°C. These phases were well crystallized and from Fig. 14c, it can be seen that the cauliflower-shaped aluminous phases were embedded in C-(A)-S-H gel. These observations are in line with what had been described by Pichon [8] for whom the late formation of C-A-S-H comes to cover the aluminous frame. Fig. 15e shows another typical micrograph of L—PYR at 50°C in which the interstitial mass (between crystals) was fulfilled with C-(A)-S-H phases. At 20°C, Fig. 14f shows an interesting micrograph of CC surrounded by an AFm phase (Al/Ca ~ 0.5) assumed to be monocarboaluminate.

The microstructure of L—MS at 50°C is illustrated in Fig. 14g and Fig. 14h. Compared to 20°C (Fig. 14b), the interstitial mass (between the quartz crystals) was much denser. The higher magnification of Fig. 14h made easier to see that quartz grains were trapped in a massive gel-like microstructure. In addition, a lot of large-sized areas interpreted as former lime particles that converted to C-(A)-S-H were observed.

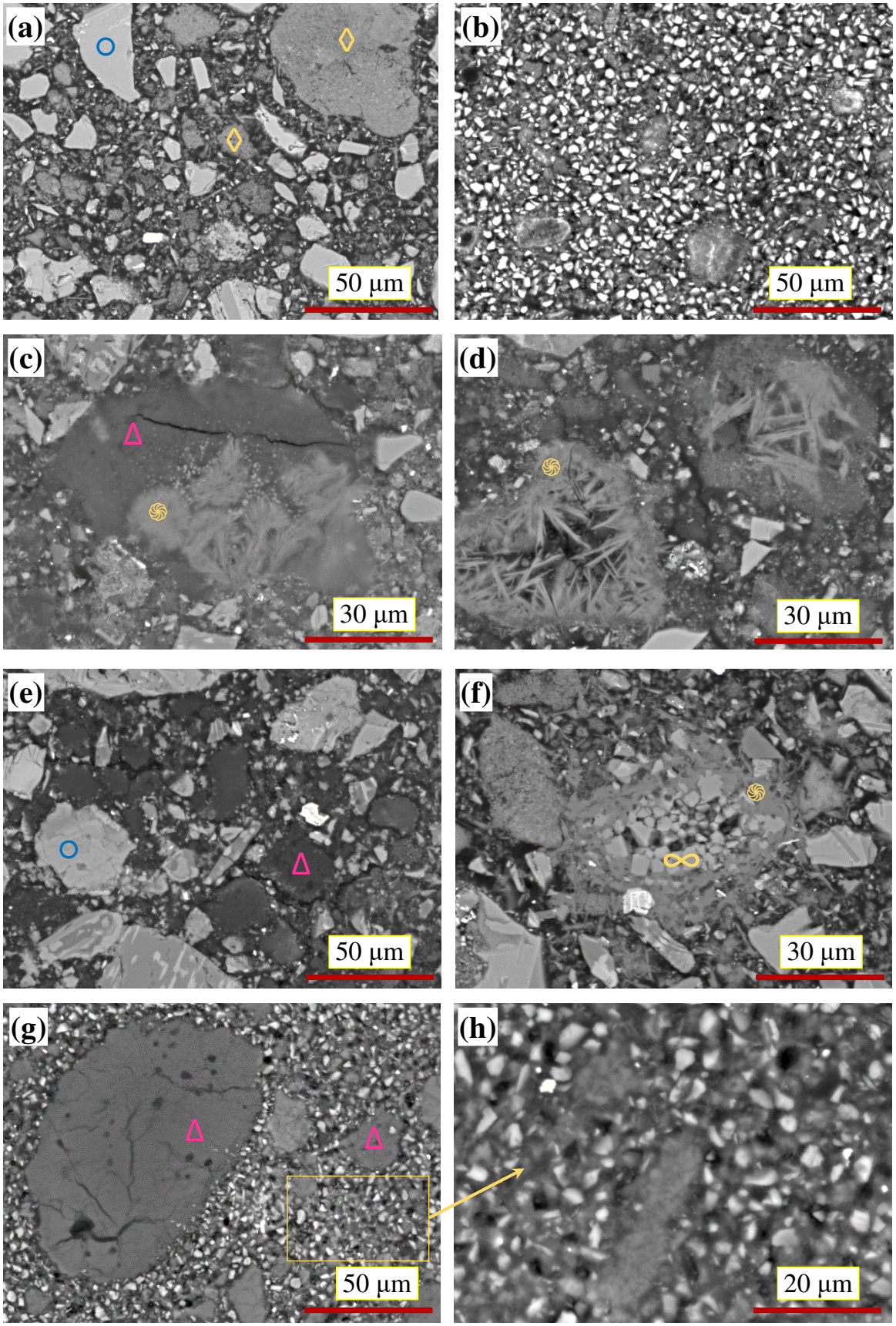

Fig. 14. BSE-SEM pictures of hardened pastes at 90 days
(a, f) L–PYR at 20°C, **(b)** L–MS at 20°C, **(c, d and e)** L–PYR at 50°C, **(g, h)** L–MS at 50°C
○ Crystal fragments, ◊ Lime cluster, ∞ Calcium carbonates, ֍AFm or HGs, Δ C-(A)-S-H gel

The punctual EDX analysis results are reported in the Ca-Si-Al ternary diagram illustrated in Fig. 15. The presence of siliceous hydrogarnets is confirmed, especially around C_3ASH_4 (katoïte). The latter is in the form of hexagonal plates (using topographic images with secondary electrons) and might justify what appeared to be needle-shaped units on polished cross sections. Some points are also more around AFm (C_4AHx) as clearly shown in Fig. 15.

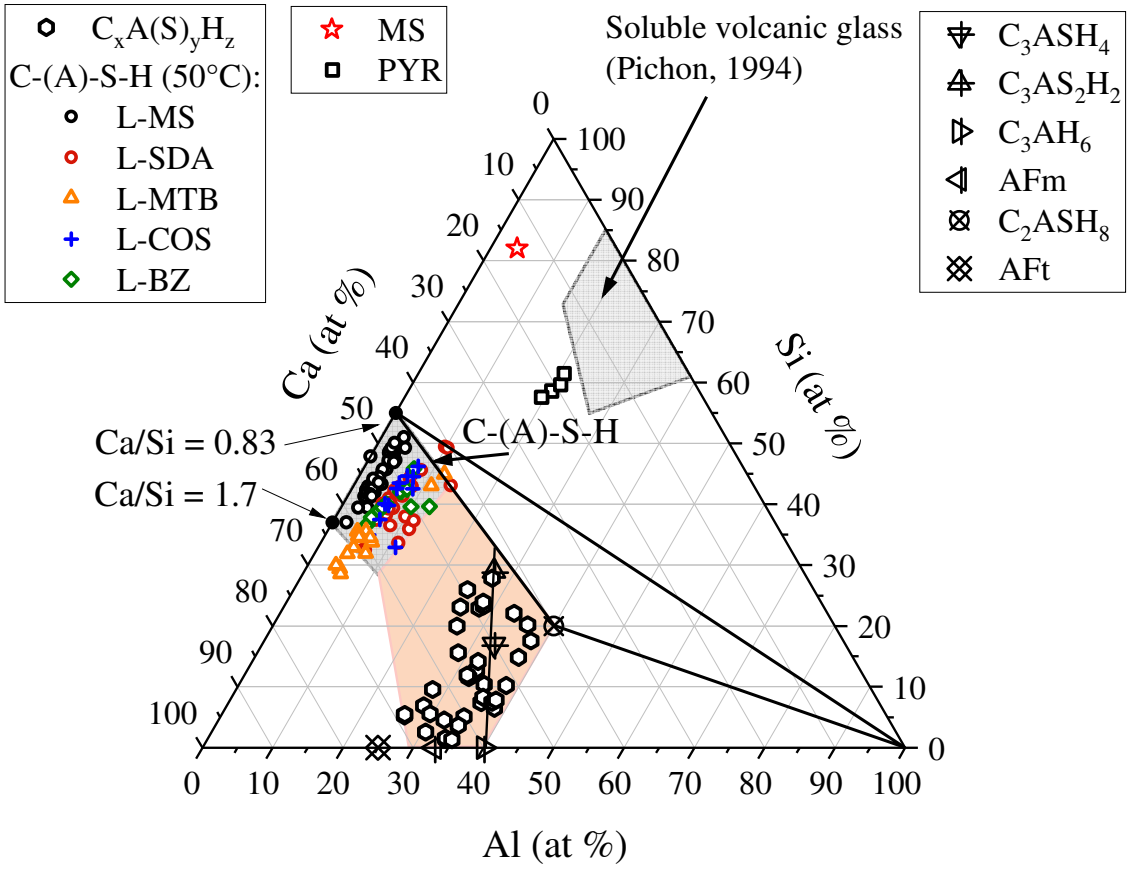

Fig. 15. Ca-Si-Al ternary phase diagram with raw materials (PYR: pyroclastics and MS: marine sediment), theoretical reaction products and pinpoint EDX analysis after 90 days of curing

EDX analysis showed a linear trend when plotting the Al/Ca ratio against the Si/Ca ratio of C-(A)-S-H as suggested in some works [56,57]. In other words, when the Ca/Si ratio decreased, the amount of incorporated aluminum increased. According to Lothenbach et al. [58], the area of C-(A)-S-H corresponds to Ca/Si ratios between 0.83 (i.e. tobermorite-like) and 1.7 (i.e. jennite-like). Only the results on samples cured at 50°C are reported for C-(A)-S-H phases since the intermixing with lime at 20°C made that task difficult. For L—SDA, L—BZ and L—COS, their mean composition was $(CaO)_{1.3}\,SiO_2\,(Al_2O_3)_\beta\,(H_2O)_Z$. It was possible to identify some C-(A)-S-H with a Ca/Si ratio around 0.8 in the case of L—SDA. On the contrary, for L—MTB, the mean Ca/Si ratio was more around 1.7. The Ca/Si ratio of calcium silicate hydrates is known to be variable in time since more and more silica is introduced into the pore solution [8,44]. It seems clear that the best compressive strength was reached for the lowest Ca/Si ratios. This was also found in the case of lime-clay mixtures [40]. For L—MS, the mean composition of C-(A)-S-H was calculated to be $(CaO)_{1.1}\,SiO_2\,(H_2O)_Z$. The Ca/Si ratio of ~ 1.1 is consistent with the study of Benezet and Benhassaine [15] about the reactivity of quartz powders. As expected, the aluminum content was almost insignificant as seen in Fig. 15.

Furthermore, it is interesting to note that points resulting from EDX on C-(A)-S-H phases were on the line between the composition of raw materials and CH (lower left corner of the ternary diagram, Fig. 15).

Since C_4AcH_{11} was quickly formed (after 7 days) for both curing temperatures, it can be assumed a zero contribution of it to the strength. The contribution of siliceous hydrogarnets highlighted by TGA, XRD and EDX is more uncertain but the conversion of C_4AH_{13} into C_3AH_6 may lead to an increase in porosity and loss of strength. In the present paper, their early formation did not prevent the L—SDA to reach 3.3 MPa after 7 days at 50°C. The strength development is mainly provided by the growth of C-S-H. However, it is necessary to consider the calcium aluminate phases for the lime combination.

3.5. Porosity investigation

The pore size distribution of pastes after 90 days of hardening at 50°C is reported in Fig. 16.

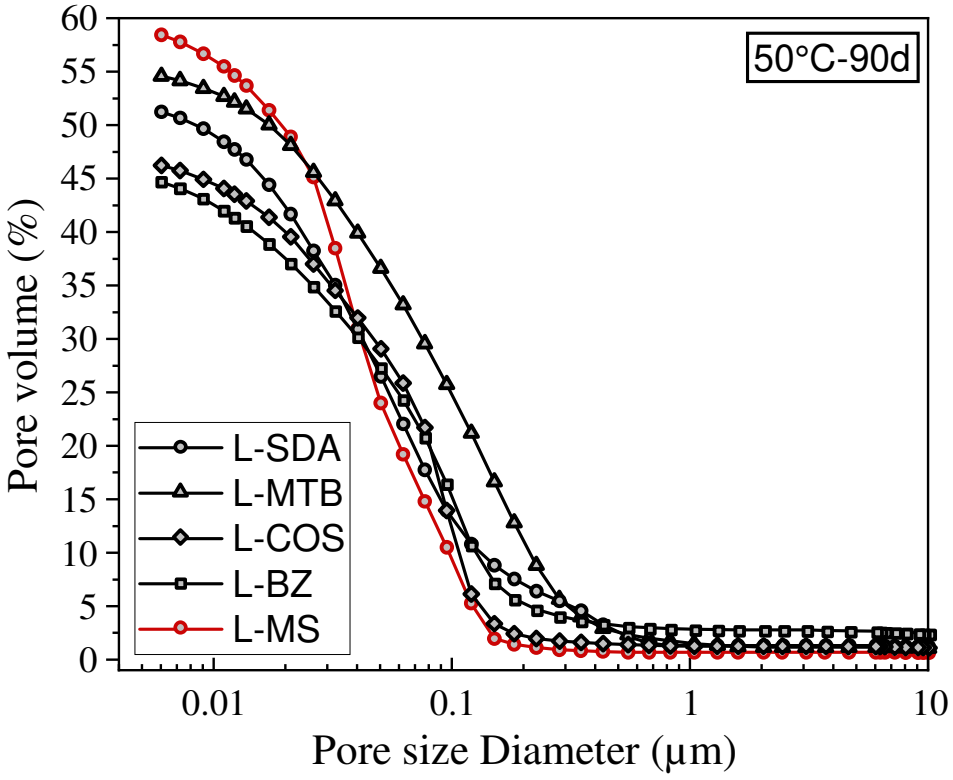

Fig. 16. Pore size distribution of hardened pastes after 90 days of curing at 50°C

The total porosity was in the range of 45 to 55 vol.% for L—PYR and slightly less than 60 vol.% for L—MS. A strong correlation between the water-on-powder mass ratio and the total porosity is clearly observed in Fig. 16. This is due to a higher capillary porosity when the water content increases [29,30,59]. It is well known that the water-on-powder mass ratio is an important parameter for which a little variation can induce large changes in the total porosity [60]. The total porosity may be affected by many factors such as curing conditions, age and degree of hydration [60]. The absolute strength of lime-pozzolan pastes do not only depend on their total porosity but also on the phase constitution (kind and relative volume of hydration products, unreacted phases, etc.) [61]. For instance, in the case of L—MS, the total porosity was 57.8 vol.% at 20°C and 58.4 vol.% at 50°C whereas the compressive strengths of pastes were 0.8 MPa and 12.1 MPa respectively. This result is attributed to the different nature of the reaction products (density, microstructure) depending on the curing conditions.

To investigate the effect of curing temperature, differential distributions are reported in Fig. 17. The latter shows the porosity refinement for the pastes cured at 50°C (Fig. 17b) compared to those cured at 20°C (Fig. 17a).

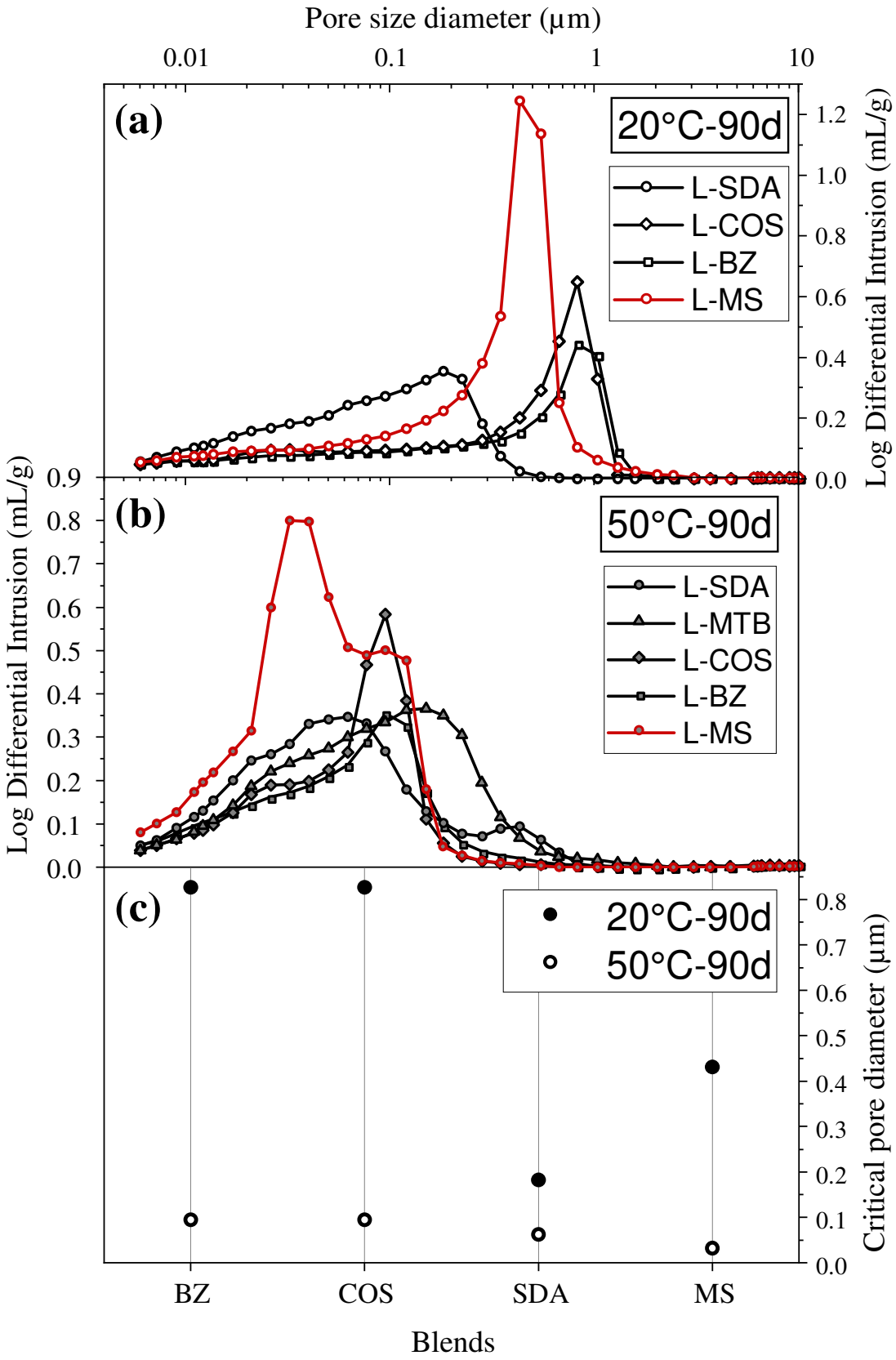

Fig. 17. Differential distribution of mercury intrusion after 90 days of curing **(a)** 20°C, **(b)** 50°C **(c)** Critical pore diameter reported for the different blends depending on the curing temperature

The porosity moved towards smaller sizes. This porosity refinement contributes to the densification of the granular skeleton and consequently to the compressive strength. According to

Cheng et al. [62], a pore size over 0.2 µm would correspond to so-called harmful pores. It can be seen in Fig. 17 that the amount of these coarse pores was significantly reduced for pastes cured at 50°C compared to those cured at 20°C. The porosity refinement is indeed confirmed in Fig. 17c where the critical pore diameter is reported for each blend. The results clearly show a lower critical pore diameter for the pastes cured at 50°C, highlighting the infilling of pores by the hydration products. Furthermore, it is interesting to note that in the case of L—SDA, the difference between the two critical pore diameters (at 20°C and 50°C) was significantly lower compared to the pastes including the other pyroclastics. This is consistent with the compressive strength results since SDA has always been the most reactive at 20°C. The porosity refinement of L—MS should not be compared to that observed in the case of L—PYR since the total porosity and the pore size distribution depend on the origin and the nature of the material. However, it is still possible to underline the denser microstructure of L—MS in relation to its smallest critical pore diameter. L—MTB is not reported in Fig. 19c since no hardening was observed at 50°C.

Fig. 18 shows the pore size distribution of pastes combining lime and either one of the pyroclastics (COS) or the marine sediment after 90 and 180 days of curing depending on the curing temperature. The variation of the total porosity between 90 days and 180 days of curing for a given blend is expected to be low since it was shown that the total porosity of cement pastes does not change a lot beyond 14 days with a much faster reaction kinetics [29,30]. At 20°C, the curve of cumulative pore volume for L—COS was strongly shifted to the left from 90 days to 180 days whereas at 50°C the pore size distributions were nearly overlapped. This confirms that the reaction proceeds very slowly at 20°C and suggests that porosity refinement came to an end at 50°C. For L—MS, there is scope for greater refinement beyond 180 days at 20°C. In addition, an evolution of the median pore diameter can be observed at 50°C (i.e. 0.045 µm after 90 days versus 0.03 µm after 180 days). Therefore, the porosity refinement of L—MS continues to develop beyond 90 days of curing.

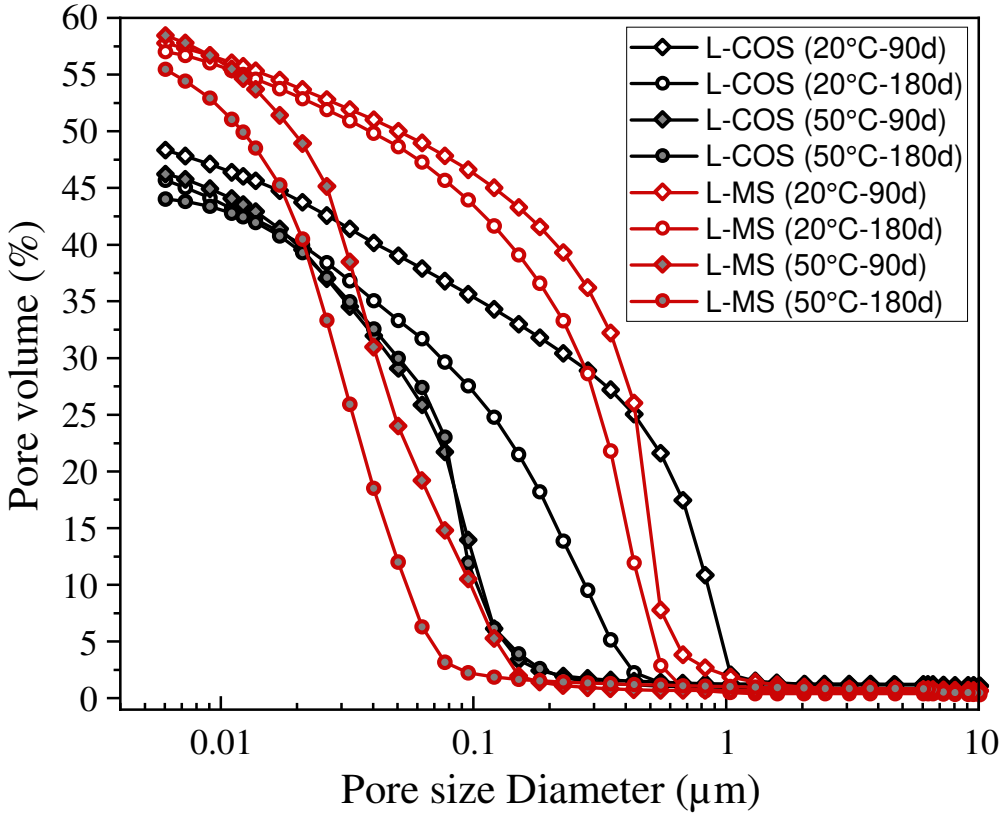

Fig. 18. Pore size distributions of L—COS and L—MS after 90 days and 180 days of curing at 20°C and 50°C

4. Conclusion

Based on the different findings, the following conclusions can be drawn:

(1) The percentage of fixed lime at 50°C is clearly improved compared to that at 20°C and this applies for the marine dredged sediment as well as for the basaltic pyroclastics. At 50°C, lime combination is found to be strongly correlated with the specific surface area of ground pyroclastics.

(2) At 20°C, the percentage of fixed lime tends to level off at about 40%, except for one of the pyroclastics for which analcime was involved. It is found that fixation of lime does not necessarily lead to the hardening of the binders and this is related to the poor binding properties of reaction products formed at 20°C and at early age for heat cured samples.

(3) At 50°C, the micronized marine sediment is able to fix a substantial amount of lime. However, the hardening kinetics at the early age is very slow with a compressive strength of only 1.45 MPa after 14 days. The higher water-on-powder mass ratio and the presence of organic matter within the marine sediment should be considered. After 180 days, the compressive strength reached with this quartz-rich sediment (~70 wt.% SiO_2) is more than 12 MPa and it keeps going up. This is consistent with the porosity refinement that is still growing from 90 to 180 days. This remarkable strength gain suggests a huge apparent activation energy.

(4) By referring to Eq. 1, the micronized marine sediment shows an interesting pozzolanic reactivity under specific curing conditions i.e. saturated humidity and 50°C. Hence, it would be wrong to consider raw sediments (i.e. without calcination) as non-pozzolanic materials. In these suitable curing conditions and for advanced curing times, the reactivity of the quartz-rich micronized sediment studied herein is even of a higher intensity compared to French basaltic pyroclastics.

The next investigations will focus on the use of other marine sediments with different mineralogical compositions (different fractions of sand and fines). The ratio of lime to sediment will also be studied in a forthcoming study.

Declaration of competing Interest

The authors declare that they have no known competing financial interests or personal relationships that could have appeared to influence the work reported in this paper.

Acknowledgments

The authors would like to thank the Hauts-de-France region and the European Regional Development Fund (ERDF) for financial support.
They are also grateful to G. Potier, M. D'Helft (MIP & technical support), J. Trigallez, V. Thiery (sample preparation for SEM), D. Betrancourt (SEM-EDX) and P. Bedart (strength test & technical support).

CRediT autorship contribution statement

S. Kourtaa: Investigation, Methodology, Data curation, Writing – original draft
M. Chabannes: Conceptualization, Methodology, Investigation, Data curation, Resources, Writing – original draft, Writing – Review & editing, Validation, Supervision
F. Becquart: Resources, Writing – Review & editing, Co-supervision
N.-E. Abriak: Co-supervision

References

[1] C. Shi, Studies on several factors affecting hydration and properties of lime-pozzolan cements, Journal of materials in civil engineering (2001) 13:441-445.

[2] A. Maropoulou, A. Bakolas, E. Aggelakopoulou, Evaluation of pozzolanic activity of natural and artificial pozzolans by thermal analysis, Thermochimica Acta 420 (2004) 135-140.

[3] V. Nozahic, S. Amziane, G. Torrent, K. Saïdi, H. De Baynast, Design of green concrete made of plant-derived aggregates and a pumice-lime binder, Cement and Concrete Composites 34 (2012) 231-241.

[4] G. Escadeillas, C. Magniont, S. Amziane, V. Nozahic. Binders, in: S. Amziane, L. Arnaud, N. Challamel. Bio-aggregate-based building materials: Applications to hemp concrete, 2013, WILEY-ISTE.

[5] A. Arrigoni, R. Pelosato, P. Melia, G. Ruggieri, S. Sabbadini, G. Dotelli, Life cycle assessment of natural building materials: the role of carbonation, mixture components, and transport in the environmental impacts of hempcrete blocks, Journal of Cleaner Production 149 (2017) 1051-1061.

[6] S. Pretot, F. Collet, C. Garnier, Life cycle assessment of a hemp concrete wall: Impact of thickness and coating. Building and environment 72 (2014) 223-231.

[7] P. Rocher (BRGM). Memento roches et minéraux industriels. Ponces et pouzzolanes, R36447, 1992.

[8] H. Pichon. Le système « Pouzzolanes naturelles – chaux – eau » à 38°C et 100°C. PhD Thesis, Université Joseph Fourier, Grenoble, 1994.

[9] H. Pichon, P. Gaudon, A. Benhassaine, O. Eterradossi. Caractérisation et quantification de la fraction réactive dans les pouzzolanes volcaniques. Bulletin des Laboratoires des Ponts et Chaussées. 201, Ref. 4011, 1996.

[10] R. Snellings, G. Mertens, J. Elsen, Supplementary Cementitious Materials, Reviews is Mineralogy & Geochemistry, Vol. 74 (2012) 211-278.

[11] M. Fournier, J.-M. Geoffray. Le liant pouzzolanes-chaux. Bull. Liaison Labo. P. et Ch., 93, Ref. 2145, 1978.

[12] J. Millet, R. Hommey. Etude minéralogique de pâtes pouzzolanes-chaux. Bull. Liaison Labo. P. et Ch., 74, Ref. 1535, 1974.

[13] D.H. Krinsley, I.J. Smalley. Sand: The study of quartz sand in sediments provides much more information about ancient geological environments, American Scientist 60, N°3 (1972) 286-291.

[14] U. Ludwig, H.E. Schwiete. Researches on the hydration of trass cements. In: Proceedings of the fourth International Congress on the chemistry of cement, Washington, 1960. US Monograph (1962) 43(2): 1093-100.

[15] J.C. Bénézet, A. Benhassaine, Grinding and pozzolanic reactivity of quartz powders, Powder Technology 105 (1999) 167-171.

[16] S. Diamond, J.L. White, W.L. Dolch, Transformation of clay minerals by calcium hydroxide attack. Clay and clay minerals 12 (1963) 359-379.

[17] C. Shi, R. L. Day, Comparison of different methods for enhancing reactivity of pozzolans, Cement and Concrete Research 31 (2001) 813-818.

[18] C. Shi, R. L. Day, Chemical activation of blended cements made with lime and natural pozzolans, Cement and Concrete Research 23 (1993) 1389-1396.

[19] C. Shi, R. L. Day, Pozzolanic reaction in the presence of chemical activators Part I. Reaction kinetics, Cement and Concrete Research 30 (2000) 51-58.

[20] C. Shi, R. L. Day, Acceleration of strength gain of lime-pozzolan cements by thermal activation, Cement and Concrete Research 23 (1993) 824-832.

[21] F. Massaza. Pozzolana and pozzolanic cements, in: P. Hewlett, Ed., Lea's Chemistry of Cement and Concrete, Arnold, London, 1998, pp. 471-631.

[22] F. Audubert, M-T. Conan, R. Maherault. La commission de volcanisme dans le Devès. SAGA Information – N°317, 2012.

[23] P. Domone, C. Hsi-Wen, Testing binders for high-performance concrete, Cement and Concrete Research 27(8) (1997) 1141-1147.

[24] E. Akgül, L. Tanaçan, Evaluation of the pozzolanic activity of the earth of Datça as a building material, International Journal of Architectural Heritage: Conservation, Analysis, and Restoration, 5:1 (2011) 1-26.

[25] J. Zhang, G.W. Scherer, Comparison of methods for arresting hydration of cement. Cement and Concrete Research 411 (2011) 1024-1036.

[26] K. Scrivener, R. Snellings, B. Lothenbach. A practical guide to microstructural analysis of cementitious materials. CRC Press Taylor & Francis Group, Boca Raton, 2016, pp. 419–444.

779 [27] A. Bakolas, E. Aggelakopoulou, Pozzolanic activity of natural pozzolan-lime pastes and
780 physicomechanical characteristics, Journal of Thermal Analysis and Calorimetry 135 (2019) 2953-2961.
781 [28] T. Kim, J. Olek. Effects of sample preparation and interpretation of TGA curves on calcium hydroxide
782 in hydrated pastes and mortars. Transportation Research Record Journal of the Transportation Board,
783 n°2290, 2012.
784 [29] E. Berodier, K. Scrivener, Evolution of pore structure in blended systems, Cement and Concrete
785 Research 73 (2015) 25-35.
786 [30] E. Berodier, J. Bizzozero, A.C.A. Muller, Mercury intrusion porosimetry, in: K.L. Scrivener, R.
787 Snellings, B. Lothenbach (Eds.), A Practical Guide to Microstructural Analysis of Cementitious Materials,
788 CRC Press Taylor & Francis Group, Boca Raton, 2016, pp. 419–444.
789 [31] M. J. L. Bas, R.W. Le Maître, A. Streckeisen, B. Zanettin, A chemical classification of volcanic rocks
790 based on the Total-Alkali Silica diagram, Journal of Petrology 27(3) (1986) 745-750.
791 [32] J. Millet, R. Hommey, F. Brivot. Dosage de la phase vitreuse dans les matériaux pouzzolaniques. Bull.
792 Liaison Labo. P. et Ch. 92, Ref. 2019, 1977.
793 [33] R. Dron. L'activité pouzzolanique. Bulletin des Laboratoires des Ponts et Chaussées. 93, Ref. 2144,
794 1978.
795 [34] G. Malquori. Proc. IVth. Inter. Symposium in the Chemistry of Cements, 1960.
796 [35] R. Dron, F. Brivot. Bases minéralogiques de sélection des pouzzolanes. Bulletin des Laboratoires des
797 Ponts et Chaussées. 92, Ref. 2115, 1977.
798 [36] S. Özen, M.C. Goncuoglu, B. Liguori, B. de Gennaro, P. Cappelletti, G.D. Gatta, F. Iucolano, C.
799 Colella, A comprehensive evaluation of sedimentary zeolites from Turkey as pozzolanic addition of cement
800 and lime based binders, Construction and Building Materials 105 (2016) 46-61.
801 [37] B. Uzal, L. Turanli, H. Yücel, M.C. Göncüoglu, A. Culfaz, Pozzolanic activity of clinoptilolite: A
802 comparative study with silica fume, fly ash and a non-zeolitic natural pozzolan, Cement and Concrete
803 Research 40 (2010) 398-404.
804 [38] R.L. Day. Pozzolans for use in low-cost housing. State of the Art Report for the International Research
805 Centre, Ottawa, Canada. University of Calgary, 1990.
806 [39] J. Costa, F. Massazza. Natural pozzolans and fly ashes: analogies and differences. In: Proceedings of
807 Symposium on effects of fly ash incorporation in cement and concrete, Boston. Materials Research Society,
808 191 (1981) pp. 134-144.
809 [40] R. Walker, S. Pavia, Physical properties and reactivity of pozzolans, and their influence on the
810 properties of lime-pozzolan pastes, Materials and Structures (2011) 44:1139-1150.
811 [41] N. I. F. Mbowou, S. Owona, B. Chako Tchamabe, J. Lissom, B. Lanson, G.E. Ekodeck, Mineralogy
812 and geochemistry of pozzolans from the Tombel Plain, Bamileke Plateau, and Noun Plain monogenic
813 volcanoes in the central part of the Cameroon Volcanic Line, Acta Geochimica 39 (2020) 830-861.
814 [42] H. Maraghechi, M. Maraghechi, F. Rajabipour, C.G. Pantano, Pozzolanic reactivity of recycled glass
815 powder at elevated temperatures: Reaction stoichiometry, reaction products and effect of alkali activation,
816 Cement and Concrete Composites 53 (2014) 105-114.
817 [43] C.G. Ruff. Time-temperature-strength-reaction product relationships in lime-bentonite-water mixtures,
818 1965, Retrospectives Thesis and Dissertations, 4022.
819 [44] H. F. W. Taylor. The chemistry of Cement Hydration. In: J. E. Burke, ed. Progress in Ceramic
820 Science, Vol. 1, pp. 95-145. Pergamon Press, New-York, 1961.
821 [45] J. Paya, J. Monza, M.V. Borrachero, S. Velazquez. Evaluation of the pozzolanic activity of fluid
822 catalytic cracking catalyst residue (FC3R). Thermogravimetric analysis studies on FC3R-Portland cement
823 pastes. Cement and Concrete Research 33 (2003) 603-609.
824 [46] C. Shi, R. L. Day. Pozzolanic reaction in the presence of chemical activators Part II. Reaction products
825 and mechanism. Cement and Concrete Research 30 (2000) 607-613.
826 [47] P. Ubbriaco, F. Tasselli, A study of the hydration of lime-pozzolan binders, Journal of Thermal
827 Analysis, Vol. 52 (1998) 1047-1054.
828 [48] A.F.N. de Azeredo, L.J. Struble, A.M.P. Carneiro. Microstructural characteristics of lime-pozzolan
829 pastes made from kaolin production wastes. Materials and Structures 48 (2015) 2123-2132.
830 [49] T. Matschei, B. Lothenbach, F. P. Glasser. Thermodynamic properties of Portland cement hydrates in
831 the system CaO-Al_2O_3-SiO_2-$CaSO_4$-$CaCO_3$-H_2O. Cement and Concrete Research 37 (2007) 1379-1420.
832 [50] M. S. Morsy. Effect of temperature on hydration kinetics and stability of hydration phases of
833 metakaolin-lime sludge-silica fume system. Ceramics - Silikaty 49(4) (2005) 225-229.

[51] A. Sepulcre-Aguilar, F. Hernandez-Olivares. Assessment of phase formation in lime-based mortars with added metakaolin, Portland cement and sepiolite, for grouting of historic masonry. Cement and Concrete Research 40 (2010), 66-76.
[52] D. Damidot, F.P. Glasser. Investigation of the $CaO-Al_2O_3-SiO_2-H_2O$ system at 25°C by thermodynamic calculations. Cement and Concrete Research 25 (1995) 22-28.
[53] B.Z. Dilnesa, B. Lothenbach, G. Renaudin, A. Wichser, D. Kulik. Synthesis and characterization of hydrogarnet. Cement and Concrete Research 59 (2014) 96-111.
[54] W. Sha. Differential scanning calorimetry study of the hydration products in Portland cement pastes with metakaolin replacement. Advances in Building Technology, Vol. 1 (2002) 881-888.
[55] G. Mertens, R. Snellings, K. Van Balen, B. Bicer-Simsir, P. Verlooy, J. Elsen. Pozzolanic reactions of common natural zeolites with lime and parameters affecting their reactivity. Cement and Concrete Research 39 (2009) 233-240.
[56] J. E. Rossen, K. L. Scrivener. Optimization of SEM-EDSS to determine C-A-S-H composition in matured cement paste samples. Materials Characterization 123 (2017) 294-306.
[57] A. Gruskovnjak, B. Lothenbach, L. Holzer, R. Figi, F. Winnefeld. Hydration of alkali-activated slag: comparison with ordinary Portland cement. Advances in Cement Research 18 (2006) 119-128.
[58] B. Lotenbach, K. Scrivener, R.D. Hooton. Supplementary cementitious materials. Cement and Concrete Research 41 (2011) 1244-1256.
[59] H.-W. Reinhardt, M. Stegmaier. Influence of heat curing on the pore structure and compressive strength of self-compacting concrete (SCC). Cement and Concrete Research 36 (2006) 879-885.
[60] I. Papayianni, M. Stefanidou. Strength-porosity relationships in lime-pozzolan mortars. Construction and Building Materials 20 (2006) 700-705.
[61] J. Jambor. Relation between phase composition, over-all porosity and strength of hardened lime-pozzolana pastes. Magazine of Concrete Research, Vol. 15, No. 45, 1963.
[62] S. Cheng, Z. Shui, T. Sun, R. Yu, G. Zhang. Durability and microstructure of coral sand concrete incorporating supplementary cementitious materials. Construction and Building Materials 171 (2018) 44-53.